Modelling of an OBS profile across Storfjorden, Svalbard
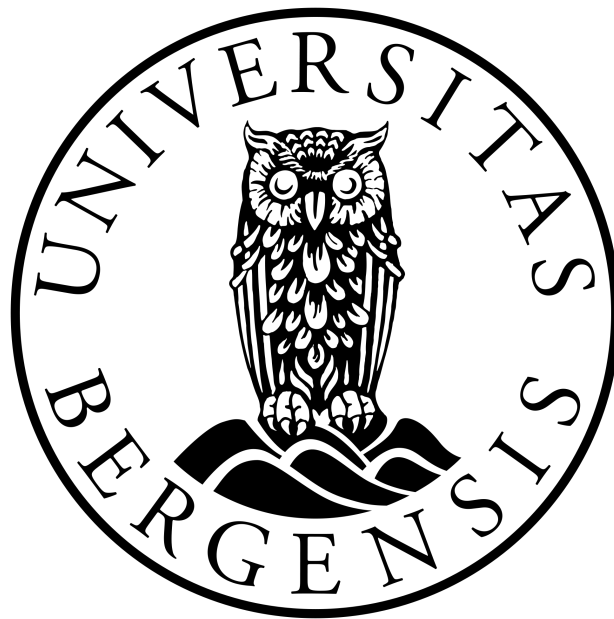
Master of Science Thesis in Geodynamics

Brede E. Hauge

Abstract

In this thesis, seismograms from eight Ocean Bottom Seismometers (OBS) have been processed, interpreted and used to obtain a 2D velocity model of a crustal transect across Storfjorden south of Svalbard through forward/inverse modelling. The aim of the study is to increase the understanding of an assumed Caledonian suture in the area, as well as recent earthquake activity. The modelling reveals a maximum Moho depth in the area predicted to be intersected by the suture. Together with a dipping down-to-west trend of the crust and mantle, this indicates the presence of an old subduction zone, supporting earlier research on the topic. From magnetic and gravitational maps of the area this suture seems to follow the trend of the Billefjorden Fault zone.

Recent seismic activity in the area is for the most part gathered in a large south-western and small north-eastern cluster. The clusters follow a SW-NE trend across Storfjorden along a proposed Tertiary shear zone and are located at the intersection between this and several major north-south oriented structures. These are mainly the suture and possible southward extensions of the Billefjorden Fault Zone and Lomfjorden Fault Zone in the south-west, and near the intersection with a possible southern extension of the Storfjorden Fault Zone in the north-east.

Acknowledgements

First of all I would like to thank my supervisor, Rolf Mjelde, for providing an interesting project, valuable support and good supervision under way. I would also like to thank my co-supervisor, Iselin Aarseth, for teaching me the software used in the thesis and constantly being available for guidance.

<div align="right">

Bergen, 20.11.2017

Brede E. Hauge

</div>

Contents

6 Conclusions 55

References 62

1 Introduction

The study area of this thesis is the north-western Barents Sea, particularly Storfjorden just south of Svalbard (Fig 1.1). Due to petroleum exploration, the south-western Barents Sea is well covered with seismic surveys, and the nature of the Caledonian Orogeny and post-orogenic development is fairly well understood (e.g. Faleide et al., 1993; Breivik et al., 1998). In the north-western Barents Sea however, fewer surveys have been conducted and only a few seismic profiles are able to constrain the top of the crystalline basement. This is due to poor resolution of conventional multi-channel seismic surveys (MCS) below the high seismic-impedance Permian carbonates (Breivik et al., 2002, 2003). In recent years, several wide angle seismic surveys have been conducted in the area in order to increase this understanding (Aarseth et al., 2017; Breivik et al., 2002, 2003, 2005; Czuba et al., 2008; Krysiński et al., 2013). One proposition common to all but one of these, is that of a Caledonian suture running across the western Barents Sea and through Svalbard. The study area of Breivik et al. (2002) is situated further east and proposes a suture across the Barents Sea through the Sentralbanken High.

In recent years, a sequence of more than 2000 earthquakes have taken place in Storfjorden south of Svalbard. These have been the subject of several studies (Pirli et al., 2010, 2013; Junek et al., 2013, 2015; Ottemöller et al., 2014), as well as a recent master's thesis by Tjåland (2017), focusing on relocation and Fault Plane Solutions (FPS) in order to understand the stress regimes under which they occurred. A general NE-SW trend have been discovered and proposed to represent a continuation of a NE-SW running shear zone put forward by Bergh and Grogan (2003). This thesis is built around the processing, interpretation and modelling of a wide-angle Ocean Bottom Seismic (OBS) profile shot across Storfjorden just south of the Svalbard archipelago. The profile cuts across the largest of two distinct clusters of the earthquake sequence, and the main objective of the thesis is to provide further insight to the nature and placement of the Caledonian suture and subsequent structures, as well as additional understanding of whether or not these structures are related to the recent seismic activity.

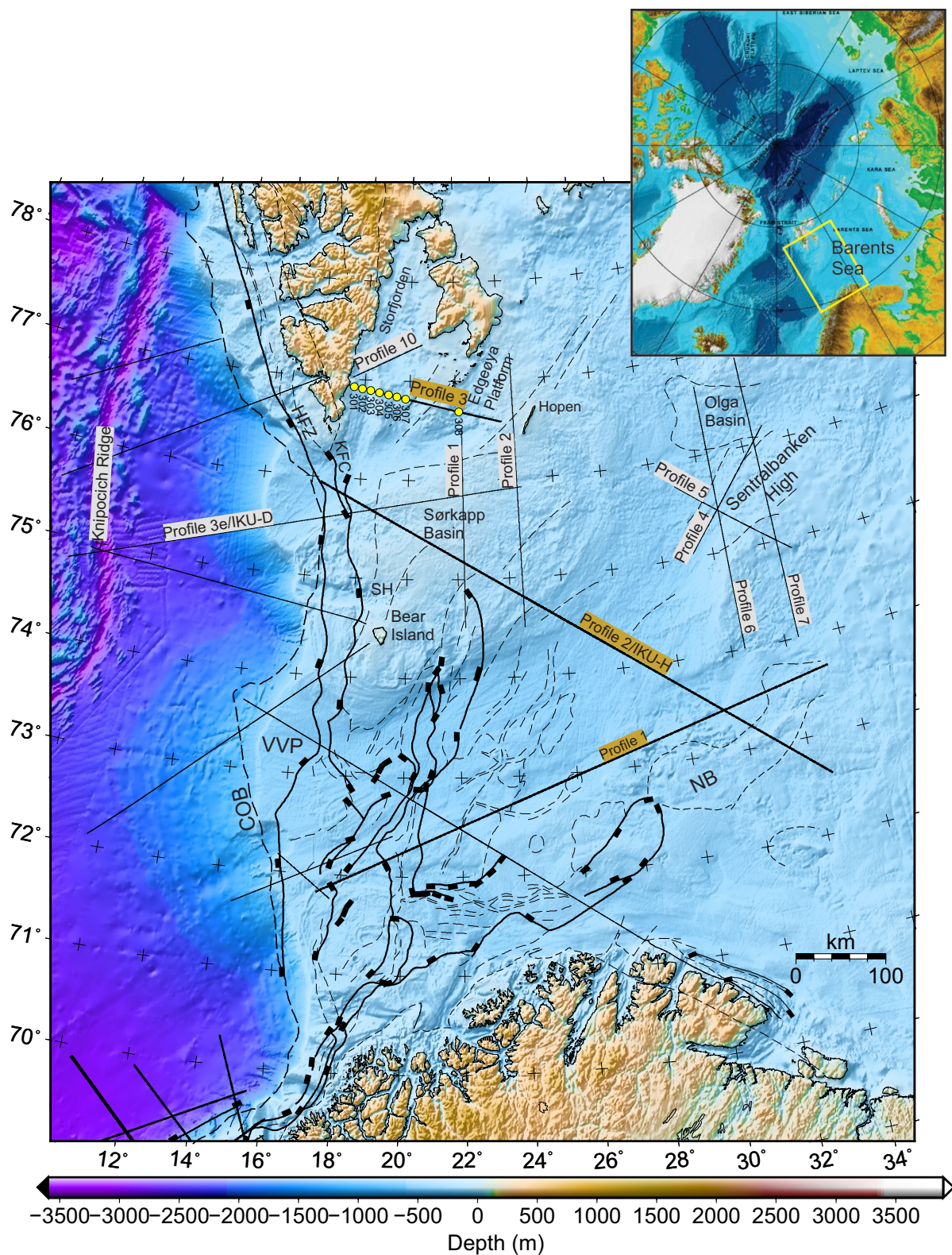**Figure 1.1:** *Location of Profile 3, subject of this thesis marked with yellow dots. Names of profiles 1 and 2 from the same 2014 survey are written in brown boxes. Profiles 4-7 are from Breivik et al. (2002). COB: Continent-ocean boundary, HFZ: Hornsund Fault Zone, KFC: Knølegga Fault Complex, SH: Stappen High, VVP:Vestbakken Volcanic Province, NB: Nordkapp Basin. Modified from Aarseth et al. (2017)*

2   Geological and tectonic setting

2.1   Caledonian development

Svalbard has a long and complex geological history. The oldest rocks with the highest degree of alteration belong to the pre-Caledonian basement. These rocks, of Precambrian (2.5 Ga) to Silurian (420 Ma) age, are exposed along the western and northern coast of Svalbard, as well as at a depth of 2-4 km in the central parts of Spitsbergen (Ramberg et al., 2007) (Fig 2.1). The structure of the crystalline basement and overlying sedimentary packages of the Barents Sea and continental margin surrounding Svalbard is heavily influenced by the Ordivician-Silurian Caledonian Orogeny and subsequent Devonian extensional collapse (e.g. Doré, 1991; Ramberg et al., 2007; Dallmann, 2015).

Uranium-lead dating of island-arc systems found exclusively over subduction zones, infers that closure of the Iapetus Ocean started as early as Late Cambrium (500 Ma). Convergence between the plates of Baltica and Laurentia eventually led to a collision involving subduction of the margin of Baltica under that of Laurentia in Silurian to Early Devonian time (430-410 Ma) (Roberts, 2003; Ramberg et al., 2007; Gee et al., 2008). The result of this is a mountain range consisting of a number of thrust-sheets piled on top of each other. The deepest of these sheets stem from Precambrian-Ordivician sediments and bedrock from Baltica, and are overlain by sheets originating from the Iapetus Ocean, and possibly even the Laurentian plate (Ramberg et al., 2007).

The Pre-Devonian rocks on Svalbard, referred to as Hecla Hoek, is commonly divided into three separate blocks or crustal fragments, called the north-eastern, south-eastern and north-western terrains, all three affected by the Caledonian Orogeny. This division is based on large differences in rock type, structural development and thermal history, in combination with several north-south oriented, regional fault-zones, shown to have both strike-slip and dip-slip movement (Fig 2.1) (Ramberg et al., 2007; Dallmann, 2015).

Marine limestones and fossils found in the north-eastern terrain are consistent

Figure 2.1: *Geological map of Svalbard from Ottemöller et al. (2014).*

with those found on north-eastern Greenland and the North-American continent, and are proposed to be affiliated with north-eastern Greenland and North-America (Ramberg et al., 2007). The north-western block is proposed to be of deep crustal origin due to the presence of mafic and ultramafic intrusions cutting through the Precambrian bedrock. The south-western block is comprised of subduction-type rocks of mid-Ordovician age (470-460 Ma) and metamorphosed carbonate rocks (flysch) of mid-Silurian age (435-425 Ma), pointing to the existence of a subduction zone in the area at the time (Ramberg et al., 2007).

Different hypotheses have been proposed concerning the orientation of the Caledonian structural trends and the location of the Iapetus Ocean suture. A memoir by Harland et al. (1997), the result of a large number of publications regarding Svalbard's geology published after the Second World War, suggested that the archipelago was divided into three blocks prior to the Caledonian Orogeny. The south-eastern terrain was located to the north,- the south-western terrain to the north-east,- and The eastern terrain to the east of Greenland. Sideways movements relative to each other of about 1000 km ensued in Late Devonian (372-358 Ma), bringing the blocks to their Late Mesozoic ($\sim$ 145 Ma) position (Fig 2.2 B). Gee and Page (1994) suggests an orthogonal compression of Laurentia and Baltica in the Silurian resulting in both compressive and transpressive forces, and movement to its Late Mesozoic position through escape tectonics (Fig 2.2 C). The closure of the Iapetus Ocean is in both models believed to be located along a north-east trend through the Barents Sea, supported by Breivik et al. (2002).

Closure of the Iapetus Ocean along a trend through Svalbard has also been proposed (e.g. Breivik et al., 2003; Gudlaugsson et al., 1998). This model further postulates two branches of the Caledonian Orogeny. One north-east through the Barents Sea and one through Svalbard along western Spitsbergen, implying the existence of Barentsia, a micro-continent independent of Laurentia and Baltica. Torsvik et al. (2001) also proposes the existence of an independent micro-continent in the Early Paleozoic which collided with Greenland in Late Ordovician, before colliding again, as part of Laurentia, with Baltica in mid-Silurian.
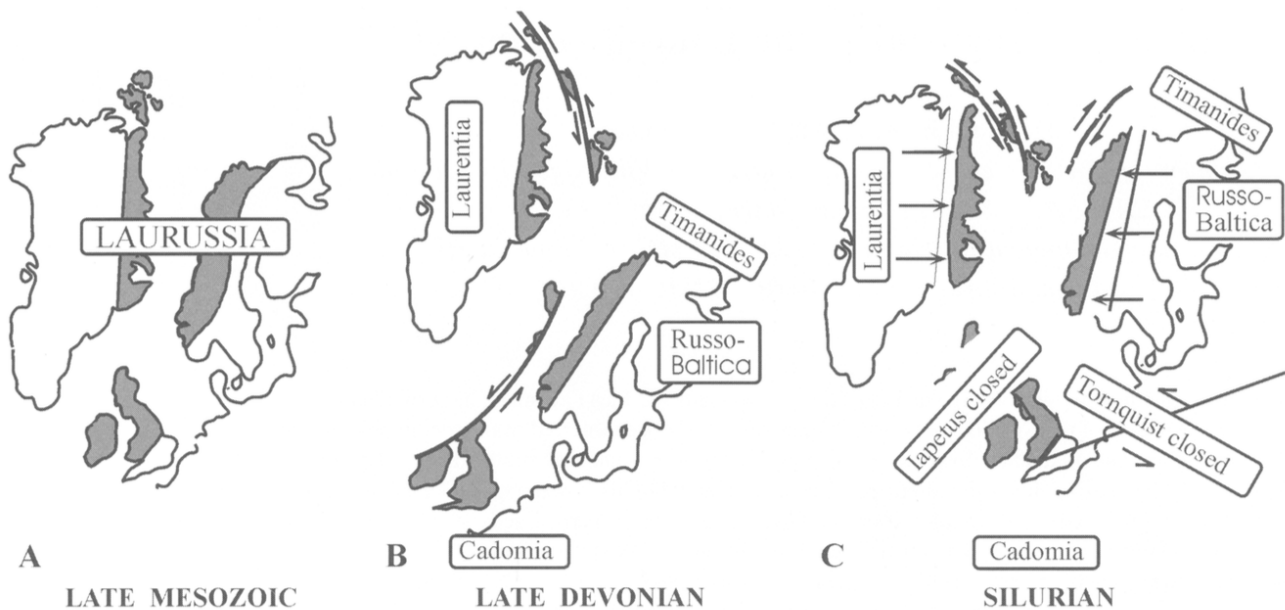
Figure 2.2: *Two transpressive models for Svalbard Caledonian terrain assembly. A: Position of Svalbard in relation to Laurussia in Late Mesozoic. B: A model of tectonic evolution involving large strike-slip movements in Late Devonian (Harland et al., 1997). C: Model involving orthogonal compression and escape tectonics during the Silurian (Gee and Page, 1994). Figure from Gee and Teben'kov (2004).*

2.2 Post-Caledonian development

After the Caledonian Orogeny, there was a shift from a compressive to an extensional tectonic regime along the Scandinavian Caledonides, where large accumulations of thrust sheets initially retreated along basal glide-zones from the previous collision, before breaking up in orogenic collapse. In the Arctic Caledonides, however, transform movements seemed to dominate (Ramberg et al., 2007). Over a long period the mountain range was exposed to weathering, and large amounts of sediments accumulated in fault-bounded Devonian molasse basins. On Svalbard, the Raudfjorden Basin and Andrè Land Basin are examples of this, bounded by the Raudfjorden Fault (RF) to the west and Billefjorden Fault Zone (BFZ) to the east (Fig 2.1) (Ramberg et al., 2007).

Spitsbergen then experienced a final compressive event in Late Devonian (~ 360 Ma), referred to as the Svalbardian event, and time-equivalent with the Ellesmerian

event in north-east Greenland and Ellesmere Island. The resulting deformation is to a large degree connected to reactivation of older, deep faults. Reactivation of the BFZ lead the basement of Ny Friesland to rise five km and being thrust to the west, and probably also north, upon Devonian molasse sediments, folding and compressing them in the process. In addition, a pull-apart basin formed along the Triungen Fault Zone (TFZ) (Fig 2.1), suggesting sinistral strike-slip movements as well as vertical ones (Worsley, 2008; Ramberg et al., 2007).

In Late Devonian-Early Carboniferous (370-347 Ma) the Barents Sea was situated just north of the equator and constituted the northern part of the Laurussian continent. From here on and through mid-Carboniferous ($\sim$ 323 Ma), crustal movements lead to widespread intra-cratonic rifting on the Barents Sea margin and Svalbard, creating several large rift-basins. Again the basin formation was constrained by faults, many of which follow old fault lines from the Caledonian Orogeny like the Billefjorden, Hornsund and Lomfjorden Fault Zones. The Nordkapp Basin, St.Jonsfjord Basin, Hornsund Basin and Billefjord Graben (Fig 1.1, 2.1) are examples of this, and became the depositional areas of several kilometre thick evaporitic sequences (Ramberg et al., 2007). The Stappen, Loppa and Sørkapp-Hornsund Highs (Fig 1.1), among others, were also tectonically active during this time (Worsley, 2008).

The period of rifting was followed by decreasing tectonism along the western margins (Ramberg et al., 2007). Subsidence rates increased, especially in the eastern area that is now the Barents Sea, as a response to the Uralide Orogeny further east (Worsley, 2008). Regional sea level rise lead to the creation of the enormous shallow Boralian Sea covering large parts of the archipelago, flooding various highs that had earlier been sources for erosion and subsequent sedimentation. Due to this lack of sedimentation, the development of a large post-rift carbonate platform followed through the Late Carboniferous-Early Permian (320-290 Ma). From mid-Permian ($\sim$ 272 Ma) the climate became colder, accompanied by a sedimentation change from warm-water carbonates to cold-water carbonates and then to clastic and organoclastic sediments. This change in climate was caused partly by the northwards movement of the Baltic plate, and partly by a change in atmospheric

circulation pattern caused by the collision of Laurussia and Gondwana, creating the Pangea supercontinent. The general submersion of the archipelago lasted to Early Cretaceous ($\sim$ 145 Ma), a period marked by relatively stable conditions and minor tectonism in the area (Worsley, 2008; Ramberg et al., 2007).

In Late Triassic to mid-Jurassic the subsidence and sedimentation rates diminished, and the major platform and basin areas present today were established. During mid-Triassic ($\sim$ 227 Ma), mudstones with an organic carbon content as high as 12 % were deposited in the Botneheia Formation on Svalbard and Steinkobbe Formation in the Barents Sea, and have been source rocks for later oil recoveries (Ramberg et al., 2007). Late Triassic saw the deposition of coal-layers on the island of Hopen (Fig 1.1) and further north-east in the Barents Sea. The Late Jurassic experienced deposition of organic rich mudstone both along the coast of Norway and in the Barents Sea, the main source rock for Norwegian hydrocarbon production. These were overlain by Cretaceous reservoir rock, but due to the platform nature of the Barents Sea at the time, the sediment thickness was much smaller than off the coast of Norway. During Late Cretaceous ($\sim$ 68 Ma), new movements and supply of heat along the north-western part of the Barents margin, associated with opening of the Arctic Ocean, caused uplift and erosion of large parts of the Cretaceous package (Worsley, 2008; Ramberg et al., 2007).

Moving into Early Paleogene ($\sim$ 66 Ma), seafloor spreading started in the Labrador Sea and Baffin Bay, advancing a movement of Greenland to the north-east with relation to Spitsbergen and the north-western Barents shelf, and transpressive and transtensional regimes initially reigned along the western Barents margin (Worsley, 2008; Dallmann, 2015).

The transpressive forces can be divided into its transform and compressive components. The transform component translated to dextral strike-slip movement along the Hornsund and Senja Fault Zones. The compressive component lead to large scale folding and thrusting of older sediments in western Spitsbergen, and to a lesser extent the Ellesmere Island and northern Greenland in Early Eocene (56-45 Ma) (Worsley, 2008; Ramberg et al., 2007).

These movements, referred to as the Eurekan Orogeny, lead to the creation of

an orogenic belt known, in the Svalbard region, as the west Spitsbergen Fold and Thrust belt (WSFTB) (Fig 2.3). A modern day analogue is the San Andreas fault in California. With estimates of crustal shortening of 10-30 km, WSFTB can be traced from the southern Barents Sea, along the west coast of Spitsbergen and west into the Greenland Sea (Worsley, 2008; Ramberg et al., 2007).

The Central Tertiary Basin (CTB) (Fig 2.1), which covers most of the central part of Spitsbergen, was formed as a foreland basin to this orogen. The basin developed a shelf area from the south-east, bounded by the Lomfjorden Fault Zone. The direction of sedimentary infill in the basin, which changed from westwards in Paleocene to eastwards in Early Eocene, is used to date the start of the WSFTB (Dallmann, 2015). The thickness of the CTB sediment packages are about 1700 m, and were deposited at or near water level. Studies on the alteration of coal layers suggest a further burial depth of 1500 meters, but these formations are today found at elevations of 1200 meters, suggesting a total uplift of Spitsbergen of about 3 km (Ramberg et al., 2007). Reasons for this uplift is attributed to several factors. Isostatic compensation took place as the Eurekan Orogeny ceased and the mountain range was eroded, and large amounts of magmatic intrusions occurred in the north-western Spitsbergen as the Greenland Sea opened in Early Oligocene, adding to the uplift. Further attribution came from erosion and run-off during the Pleistocene (2.6 Ma-11.7 Ka) ice-ages (Worsley, 2008; Ramberg et al., 2007).

In Late Eocene-Early Oligocene (35-30 Ma), spreading ceased in Baffin Bay, and the Greenland plate changed direction towards the north-east. Seafloor spreading initiated in the Greenland Sea, resulting in a divergence of the Barents Sea plate and Greenland plate. The spreading ridge is referred to as the Knipovich Ridge and the Mohns Ridge in the north and south part of the Greenland Sea respectively. The Hornsund Fault Zone which, had been the major fault of which the Barents and Greenland shelves had moved past each other, started experiencing extension, and small sedimentary basins developed along its strike (Dallmann, 2015). During the transition to seafloor spreading in the Greenland Sea, large amounts of lava were extruded in areas of stretching and thinning of the crust. Volcanic depositions with thickness in the hundreds of meters are found in the area between the Hornsund

and Senja fault zones, known as the Vestbakken Volcanic Province (VVP) (Fig 2.1) (Ramberg et al., 2007).

As previously mentioned, Neogene and Quaternary was characterized by multiple periods of glaciation. At the time of largest glacial thickness, the accumulation of ice was highest in the Barents and Kara Seas, moving outwards into Russia and over Svalbard. The archipelago was now at its current position in the uppermost north-western corner of both the Barents Sea and the Eurasian plate. 60 % of the island is today covered by glaciers, remnants of the massive ice-sheets that covered the archipelago. To the west and north, two spreading ridges are located, the Knipovich Ridge and Gakkel Ridge (Ramberg et al., 2007).
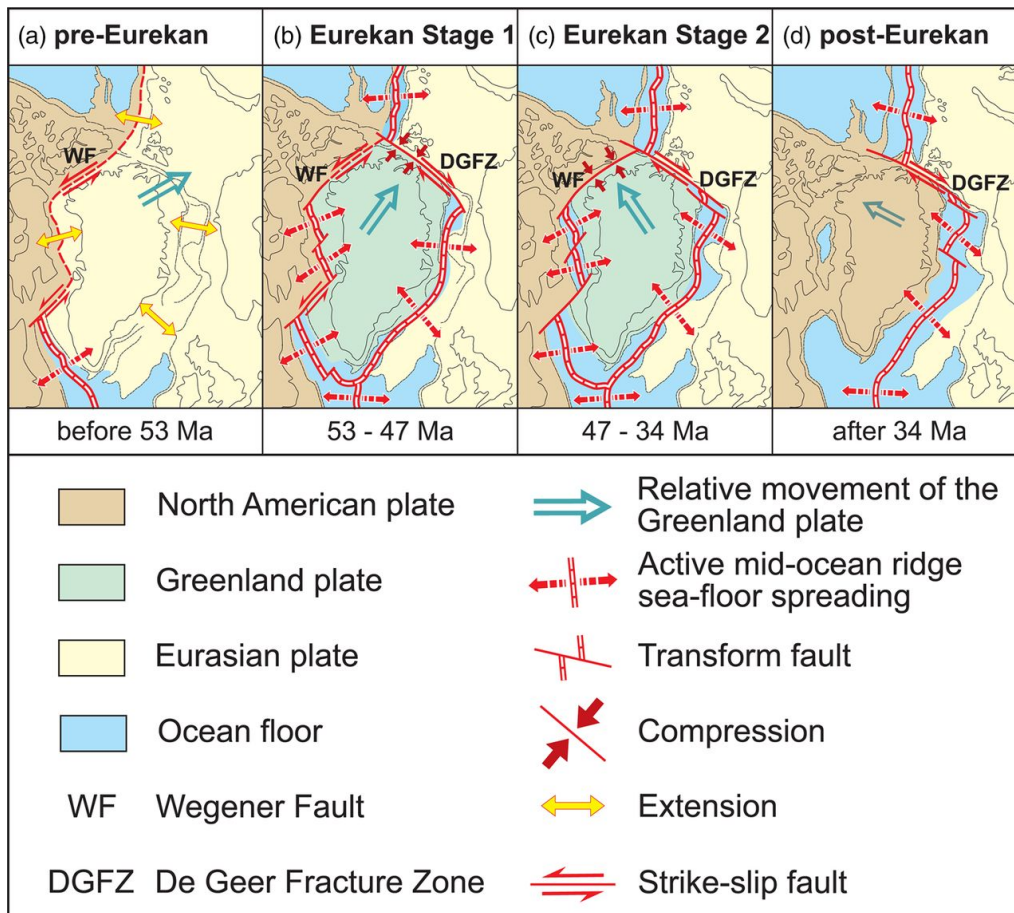
Figure 2.3: *(a): The pre-Eurekan tectonic situation. (b) and (c): Movement of the Greenland plate, first to the north-east and later to the north-west in relation to Svalbard leads to compression and dextral transpression respectively. The result is the formation of the WSFTB and adjacent foreland basin. (d): Continuing seafloor spreading eventually cause breakup between Greenland and Svalbard. Figure from Piepjohn et al. (2016).*

3 Methods

3.1 Data Acquisition

During the summer of 2014, the vessel R/V Håkon Mosby operated by the Institute of Marine Research (Bergen, Norway) through the PETROMAX program, obtained 3 Ocean Bottom seismometer (OBS) profiles in the Barents Sea. The project partners are University of Bergen (UiB), University of Oslo (UiO), IMF-GEOMAR, GFZ Potsdam and EHT-Zürich. Profile 1 is approximately 630 km and runs from north of the Tromsø Basin to the northernmost part of the Nordkapp Basin. Profile 2 is about 650 km and runs between the Knølegga Fault Complex and the Nordkapp Basin, and is described in Aarseth et al. (2017). In this thesis, the 169 km OBS data Profile 3 will be discussed. The profile runs across Storfjorden of Svalbard between the Edgeøya Platform and the Storfjorden Basin (Fig 1.1).

3.1.1 Air-guns and Ocean Bottom Seismometers

The geophysical equipment consisted of four equal sized Bolt air-guns with a total volume of 78.66 l (4800 in^3) with a 200 m shot-interval (ca. 80 s at 5 knots) and a 12 m air-gun depth. Navigation were based on the Differential Global Positioning System (DGPS). Eight digital GEOMAR Ocean Bottom Seismometers with a spacing of about 15 km (nr. 301-308) were used for Profile 3 of a total of 20 OBS's available on the vessel, recording both P-waves (vertical geophone and hydrophone) and S-waves (two orthogonal horizontal geophones) with short period sensor (4.5 Hz). The first OBS 301, as seen in (Fig 1.1) was located at 765530.62N 177248.64E and the last OBS 308, as seen in (Fig1.1) at 764126.02N 220926.09E. The shooting commenced with a "soft start", meaning that the airguns were shot one after another, with the intent that animal life would leave the area and thus avoid harm later on. Due to shallow water depth and the potential of damaging equipment no shots were fired between 0-14.55 km and 84.55-121.55 km (Bretel et al., 2014). The result of this is a transect defined in length by OBS 301 at 0 km and the first shotpoint at 169.31 km where the seismograms start at 14.55 and have a gap of no

data between 84.55 to 121.55 km.

3.1.2   Mini-streamer reflection seismic data.

Reflection data were collected simultaneously with the OBS data for all three profiles of the survey by a mini streamer (Micro Eel model, S/N ME-0008, manufactured by Geometrics) owned by the University of Bergen. This model has no depth control. The streamer had a towing distance behind the ship of 143 m, and eight channels with a spacing of 6,25 m for an active streamer length of 50 m. Both the 7th and 8th channel were broken during the acquisition of line 3. The offset from the first channel to the source were 103 m and were estimated by direct water arrival with velocity of 1473 m/s as the towing system did not have a good distance control from air guns to stern. The water velocity was found from direct water arrival deference at the first and last channel, and checked against earlier collected CTD data in the area. Recording of the mini-streamer (MS) data were done by on-board Geometrics GEODE (S/N 3699) seismic recording system. Recording time of 6.1435 s and a sample interval of 0.5 ms give a total of 12288 samples per trace. An anti-alias filter automatically adapted to sampling rate was applied (Bretel et al., 2014).

The mini-streamer reflection seismic data provided small amounts of depth penetration and contained large amounts of multiples, and was therefore only fit for constraint of the seafloor. For this task the vessels echo sounder was a simpler solution and consequently used (Mjelde, 2017). Due to time constraints, gravimetric and magnetic modelling falls beyond the scope og this thesis.

3.2   Data Processing

Preprocessing of the data was done at GEOMAR and consisted of cutting raw data into traces of 60 s, adjusting for instrumental clock drift, tying to navigation, trace normalization and conversion to SEG-Y format. The seismograms were then plotted with a reduced velocity of 8 km/s in order to compress the time scale and obtain sub-horizontal refractions from the upper mantle.

The OBS data were then corrected for physical instrumental drift. The rest of the OBS processing was done as part of this thesis at UIB/UIO and consisted of band-pass filtering, spiking deconvolution, automatic gain control, velocity reduction and debiasing. The processing steps was applied to both the hydrophone component and the vertical geophone component of each OBS. This created five independent seismograms for each of the two components for all eight OBS's, featuring different combinations of processing steps (Fig 3.1). These five are:

- Offset dependent trace weight + 4,5,12,14 Hz band-pass filter

- Spiking deconvolution + offset dependent trace weight + 4,5,12,14 Hz band-pass filter

- Automatic gain control + 4,5,12,14 Hz band-pass filter

- Spiking deconvolution + AGC + 4,5,12,14 Hz band-pass filter

- Spiking deconvolution + AGC + 3,5,6,8 Hz band-pass filter

Band pass filtering: A band-pass (BP) filter with parameters 4, 5, 12, 14 Hz was applied to increase signal to noise ratio. This type of filtering will inevitably lead to some oscillations around sharp changes in the seismic signal, commonly referred to as "ringing", and is called Gibbs Phenomenon (Fig 3.2). The filter was constructed with a trapezoid shape in order to reduce the sharpness of the signal truncation, and thus minimize this effect, though it could not remove it completely.

Another lower frequency (3,5,6,8 Hz) band-pass filter, also with a trapezoid shape, was applied to the same data. The low frequency band-pass filter destroyed

high frequency shallow arrivals, but was useful for deeper arrivals as low frequencies attenuate less. Interpretations were not made directly on the low filter seismograms, but they provided additional information assisting the interpretation.

Spiking deconvolution: Spiking deconvolution is a method of compressing a wavelet to a single spike. The processing method is used in order to filter out the reverberant parts of a signal by removing the signal train. This kind of deconvolution may increase noise at higher frequencies.

Automatic gain control: AGC is used to reduce the effects of geometric divergence or spherical spreading. A window of fixed length is chosen and the average amplitude within is calculated. A gain is then applied to all samples within the window in order to raise the average amplitude to a predetermined value. The window is then slid down the trace and the process repeated until the whole trace has been scaled up. A one second window was used on the data in this thesis to boost the far-offset arrivals.

Velocity reduction: Displaying the seismograms in reduced velocity means that the refraction arrival of interest will be displayed nearly horizontal in the seismogram. This is done by substituting the time axis for:

$$time = t - \frac{offset}{v_{red}} \tag{3.1}$$

where V_{red} is the reduction velocity. The highest commonly encountered velocity of propagation in crustal scale refraction studies is the P-wave mantle velocity of 8 km/s, and this velocity is consequently used in the seismograms. This method also limits the space needed to display the seismograms by deleting the part of the traces that have reduced time below zero.

Debiasing: Ideally the average amplitude of a trace is zero, but the trace may be shifted for several reasons. Debiasing is the process of shifting the trace back to an average amplitude of zero. This is done by measuring the actual mean amplitude of each trace and subtracting that value from every sample of the corresponding trace, bringing its mean amplitude back to zero.

Offset dependent trace weight: This step is applied to boost far-offset arrivals laterally, and consists of adding an offset-dependent gain to each entire trace. It is important in OBS seismic because large offsets means that the seismic signal have experienced increased spherical divergence already at the onset of the first arrival, and thus needs increased gain.
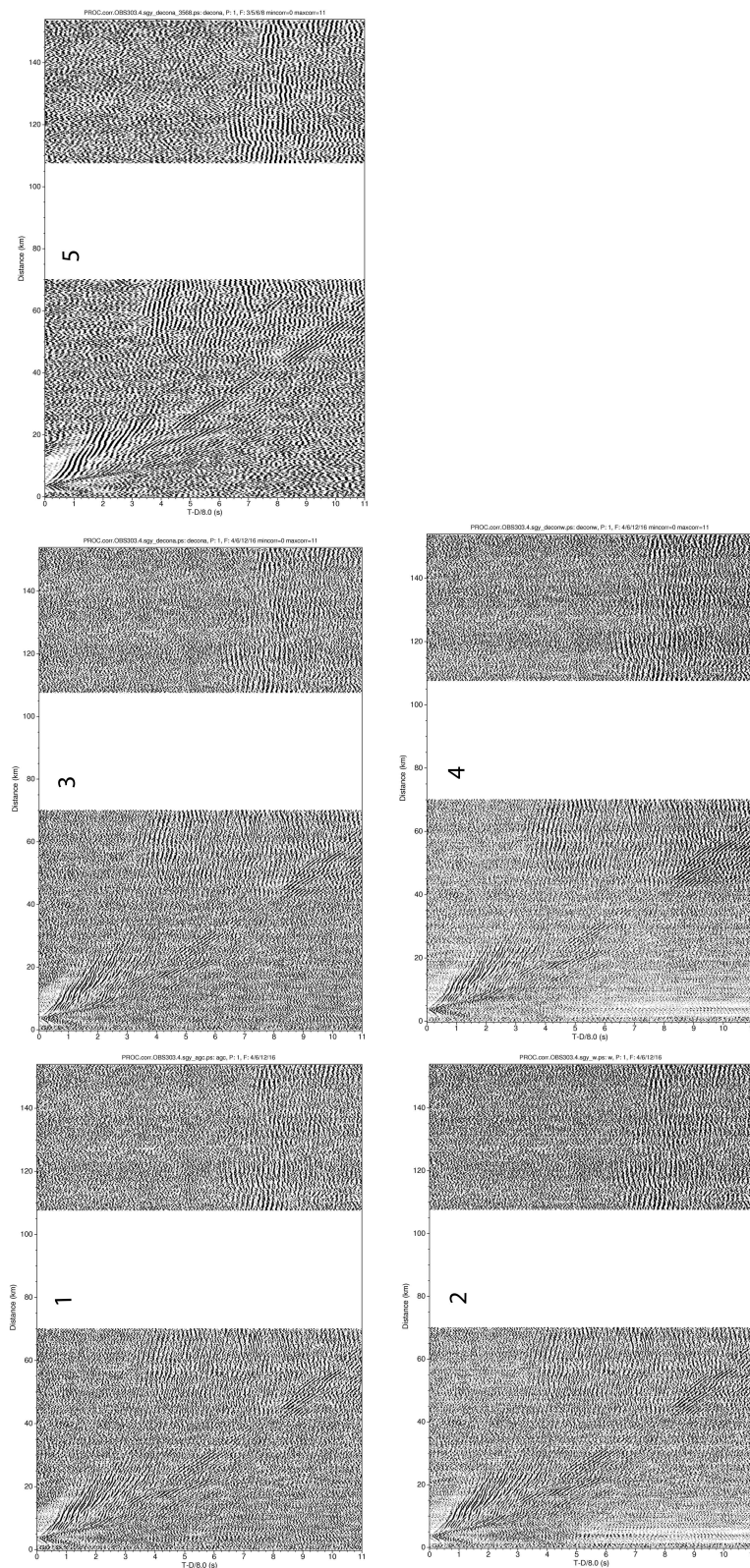
Figure 3.1: *Vertical geophone component of OBS 303 with different types of processing steps applied. 1: BP+AGC. 2: BP+Weight. 3: BP+Decon+AGC. 4: BP+Decon+Weight. 5: Decon+AGC with low frequency BP-filter.*

3.3   Interpretation

While both the hydrophone and vertical geophone component seismograms were processed for all OBS's, only one of the components for each OBS was used for interpretation as there were significant differences in quality. The hydrophone component was used for OBS 304, 306, 308 and the vertical geophone component for OBS 301, 302, 303, 305 and 307.

The processed seismograms were interpreted using the CorelDraw X7(2014) software by the Corel Corporation. The software allows for the creation of several overlapping layers, each containing different content. Choosing which layers are displayed determines the total content on the screen. Seismograms were imported into the program and a frame drawn around them in a different layer. The frame allows several differently processed versions of each seismogram to overlap each other exactly, making it possible to easily toggle between viewing each seismogram with different processing steps applied. Interpretations were drawn in a separate layer in the same manner as the frame, so that they could easily be exported as lines and curves into the modelling software. Interpreted arrivals were assumed to represent P-wave arrivals. S-wave interpretation and modelling falls beyond the scope of this thesis.

Most of the arrivals were picked on seismograms where only automatic gain control were applied. This is mainly because the gain in quality from deconvolution and weighting was slight to non-existent. Seismograms with the low frequency band-pass filter (3,5,6,8 Hz) applied were used in tandem with the normal band-pass filter (4,5,12,14 Hz) in order to exhibit general trends of dip in the seismic arrivals where such were hard to otherwise interpret.

When picking phases, an effort was made to pick the first arrival of the phase. What can be said to be the first arrival, however, is up to interpretation as well. Band-pass filtering of the data introduced a degree of ringing in the seismograms as discussed in section (3.2). Because of this, a subjective approach of balancing the very first recognisable change in signal versus the highest amplitude of the signal had to be used (Fig 3.2).
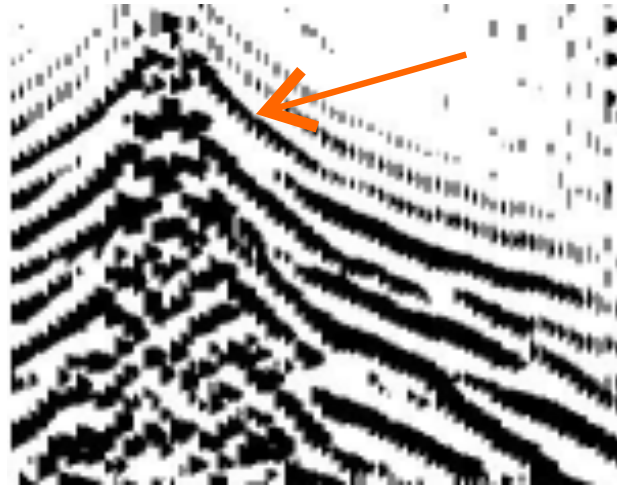
Figure 3.2: *Illustration of ringing artefacts in the seismic (Gibbs Phenomenon). Arrow points to interpreted first arrival of the phase.*

The picked arrivals were interpreted to belong to a total of eleven different seismic phases, of which ten were modelled (The Pc phase was not, but is displayed in Fig 4.7 and Fig 4.8). These are listed in Table (1) below.

Table 1: *List of abbreviations for interpreted seismic phases*

Phase	Code
P-wave refraction from sediement layer 1 (Seafloor)	Psed1
P-wave refraction from sediement layer 2	Psed2
P-wave refraction from sediement layer 3	Psed3
P-wave refraction from sediement layer 4	Psed4
P-wave reflection top basement	PcP
P-wave reflection from intra-crustal layer	PgP
P-wave reflection from within crystalline crust	PgPf
P-wave refraction top mantle	Pn
P-wave reflection from Moho	PmP
P-wave reflection from within the upper mantle	PfP

3.4   Modelling

A 2D crustal P-wave velocity model was created along the profile using Rayinvr, a ray tracing forward/inversion software developed by Zelt and Smith (1992). The software allows construction of individual layers within the model through linear lines connecting depth nodes chosen by the user. Each constructed layer initially has four velocity nodes, two on top and two on the bottom on each end of the layer. This gives the option of gradually changing the velocity within a layer both laterally and vertically. Additional velocity nodes can, as with the depth nodes, be added as needed to provide further constraint on depth of layer and velocity within and between them.

The seismograms show a horizontal axis from 0 to 154.41 km, as this is the distance the sources were active. The entire profile, however, spans 169.31 km, measured from OBS 301, north-west of the last shot-point to the first shot-point south-east of OBS 308. In order to achieve this, the crustal P-wave velocity model was created with an axis of 0 to 169.31 km, while the interpretations were imported with a framed axis from 14,55 km to 169.31 km. Within this frame OBS 301 was set to 0 km, OBS 302 to 8.31 km and so on. (Fig 3.3)
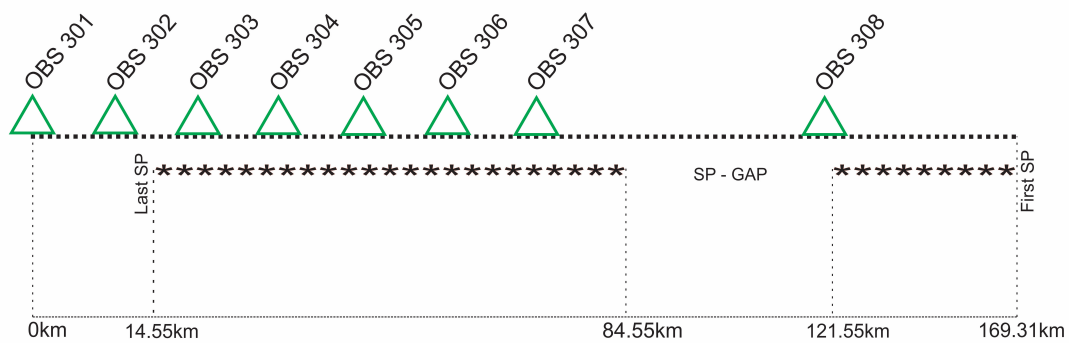

Figure 3.3: *Relative locations of Ocean Bottom Seismometers to area of active source and entire length of modelled line. The line is measured from the first Shot-point (SP) to OBS 301. No traces are shown in seismograms from 0 to 14.55 km and between 84.55 and 121.55 km (SP-GAP), as the seismic sources were not active due to shallow water depth.*

3.4.1 Modelling procedure

The initial velocity model was constrained by other nearby crustal profiles, mainly profile 1, 2 and 10 (Fig 1.1) from Breivik et al. (2005). The seafloor was constrained by echo sounder, and the water layer was given a velocity of 1.48 km/s as this is a typical P-wave velocity in arctic seas (Grad et al., 2011). For simplicity a minimum of depth nodes were used in the initial model building and rather inserted as needed. Velocity nodes were inserted along the model corresponding with the distance of each of the eight OBS's as well as at each endpoint. In a few instances additional velocity nodes were introduced in addition to these, but this was generally not needed.

The modelling procedure was conducted in a layer stripping method, where the depth,- and velocity nodes of the layers were constrained one by one with increasing depth from the seafloor to the upper mantle. The process of constraining each layer consisted of changing the values and placements of the depth and velocity nodes of the layer until the modelled arrivals from the layer gave as good a fit as possible with the interpreted arrivals on the seismograms.

The modelling software allows an arrival to be modelled as a reflected wave, head wave or diving wave. Emphasis was made to model as many arrivals as possible as head waves or diving waves. The reason for this is that these provide more information on the velocity gradient of the model through their dip. Still, secondary arrival reflections were also modelled from most of the seismograms. These reflected arrivals become important as the gap of information in the seismograms, mentioned in section (2.1.1) and (2.4), made first arrivals from most of the middle part of the crustal model difficult to obtain.

4 Results

4.1 P-wave modelling

The final crustal velocity model was separated into eight layers including the seafloor (Fig 4.1). The data quality was generally good, with the exception of OBS 301 (Fig 4.2), which provided limited quality in the shallow section, and OBS 302 (Fig 4.3) which did not provide any useful data in the deeper sections below about four km.

Direct arrivals from the water layer were omitted. Seafloor depth varies from a maximum of about 200 meters to a minimum of 40 meters constrained by bathymetry. The shallowest areas are to the very end of the profile in the north-west direction and 100 km along the profile across the Edgeøya platform.
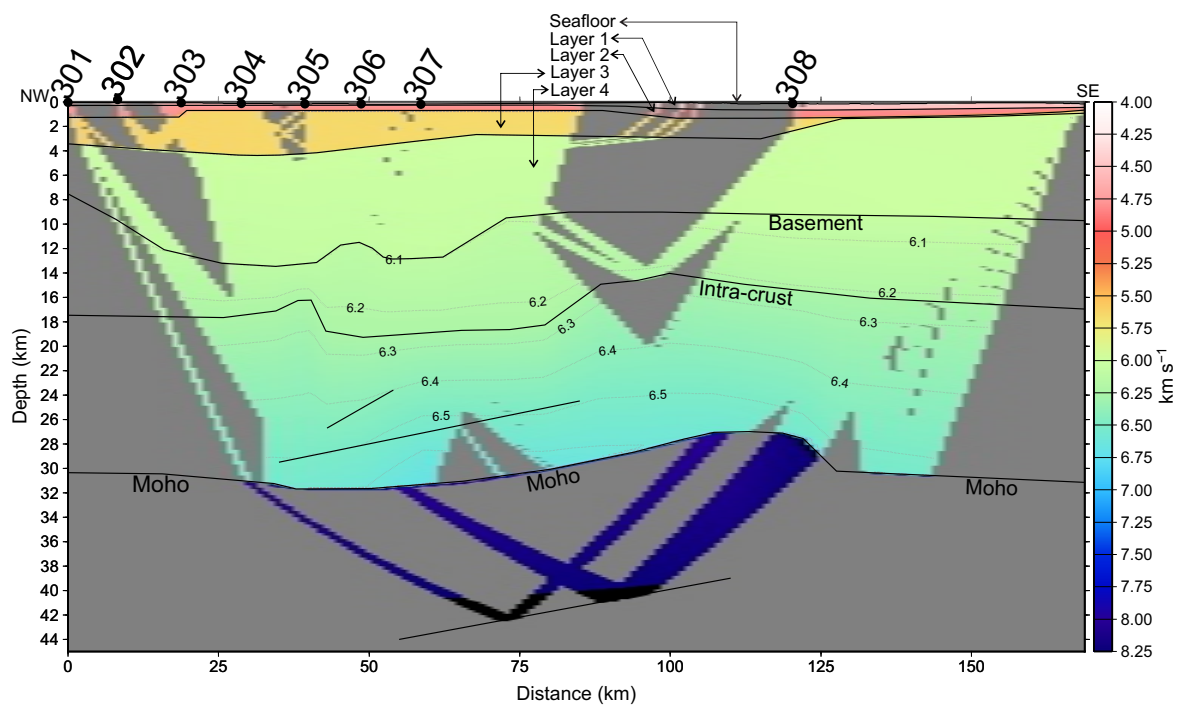

Figure 4.1: *Velocity grid of the model. OBS locations along the transect displayed on top.*

- Layer 1 velocity was constrained by all of the OBS's with the exception of OBS 301 (Fig 4.2) and OBS 302 (Fig 4.3). The layer was given a horizontally even, but vertically graduated velocity from 4.50 km/s at the top to 4.55 km/s at the bottom. The layer is thin, ranging from a thickness of approximately 100 meters in the centre of the profile to about 500 meters to the south-east. The depth to the bottom of the layer is about 300 meters in the range 0-80 km along the profile, then increasing to 690 meter at 125 km distance before decreasing again to 440 meter at the south-eastern end (Fig 4.1). Refractions from the top of Layer 1 was quickly masked by arrivals from the underlying layers. As a result, the interpreted and calculated rays are very short, making it hard to accurately constrain the velocity.

- Layer 2 is modelled by refraction arrivals on all of the seismograms except OBS 301 (Fig 4.2) and OBS 302 (Fig 4.3). The arrivals are traceable through the onset of arrivals from underlying layers for offsets from 10 to 30 km, providing a good constraint on the P-wave velocity in the layer. A P-wave velocity increasing slightly from 4.75 km/s in the north-west to 4.80 km/s in the south-east, gave a reasonably good fit to interpreted arrivals. A slightly higher velocity of 4.85-4.90 km/s gave a better fit, but inhibited the tracing of rays from underlying layers. There is a velocity increase of 0.5 km/s from the top to the bottom of the layer. The thickness is greatest in the north-western and south-eastern ends of the profile. At a distance of 0-20 km the depth is about 1.26 km before it reduces to a plateau of 720 meter from 20 km to 89 km. Then the depth again increase in a similar way to the layer above.

- Layer 3 differentiates itself from the overlaying layers by an increase in thickness and velocity. The upper velocity of the layer is constrained by refraction arrivals from all OBS's apart from OBS 301 (Fig 4.2). The bottom of the layer is constrained by refraction arrivals from all OBS's, and its depth varies greatly from 4.4 km at a distance of 32 km along the profile to almost pinch-out at 930 meters at the south-eastern end. The corresponding thickness respectively is 3.7 km and about 0.2 km. There is a sharp increase in velocity from Layer

2, to 5.6 km/s in the north-western end of the profile, increasing to 5.65 in the south-eastern end. The vertical velocity increase from top to bottom of the layer is zero from the north-western end up until a distance of 49 km, where the velocity at the bottom of the layer increase from 5.65 to 5.70 at the south-eastern end. The lower layer velocity is not well constrained.

- The velocity of Layer 4 is constrained by head waves and refracted waves on all of the OBS's, with offsets up to 70 km on OBS 301 (Fig 4.2) and OBS 302 (Fig 4.3). As with layer 3, a significant increase in velocity is introduced in layer 4, and a uniform upper layer velocity of 6.0 km/s gives a good fit with the interpreted arrivals on most of the seismograms. The lower velocity of the layer decrease from 6.10 km/s in the north-western end to 6.0 km/s in the south-eastern end of the profile, though this is only constrained by a few reflection arrivals from the basement and rays passing through from underlying layers. The layer is at its thickest approximately 20-60 km and 130-169 km along the profile. While the north-western thickness is related to increasing depth to the underlying basement, the south-eastern is associated with a decrease in the depth of the top of Layer 4 itself. The depth of the layer is poorly constrained with short offset arrivals from only OBS 306 (Fig 4.7) and 307 (Fig 4.8).

- The initial layer geometry of the basement (Layer 5) was adopted from Breivik et al. (2005), who again based the basement mostly on the reflection seismic profile SVA-1. The interpretation of this layer as the basement is based on the same article and supporting reflection seismic, as well as the upper layer velocity of 6.11 km/s in the north-west and 6.05 km/s in the south-east, found to fit in the model. The south-eastern part of the profile lacks arrivals from the basement, and without any constraint the layer is drawn almost horizontally to the end. The velocity constraint is based on arrivals passing through from underlying layers.

- Layer 6 is interpreted as an intra-crustal layer with its depth constrained by reflected arrivals from OBS's 304-308. There are no refractions constraining

upper or lower velocity, but arrivals from deeper layer passing through give a general average velocity of the model as a whole. Refracted arrivals from the bottom of the layer (Pc-phase) were interpreted on OBS 306 (Fig 4.7) and OBS 307 (Fig 4.8) due to a change in dip similar to that from deeper layers, but could not be modelled by the software. Large offset arrivals from this layer are of good quality on OBS 306 (Fig 4.7) and 307 (Fig 4.8), but cuts off abruptly at a distance of about 140 km, suggesting a hindrance to seismic waves in the upper south-eastern end of the profile.

- Moho (Layer 7) is well constrained throughout the profile by small to large offset reflections on OBS 303-308 (Fig 3.3 - 3.8) and refractions on OBS 303-305 (Fig 3.3 - 3.5). An upper mantle velocity of 8.0 km/s provides a good fit to data in the north-western end to the middle of the profile. From there the velocity rapidly increase to 8.20 km/s over a distance of 10 km. The Moho surface is fairly well constrained from 30 km to 140 km. The maximum depth of 31.7 km is found 38 km along the profile, with gradual shoaling on both sides. The depth at 0 km is 30.4 km, and the shallowest is found at a distance of 118.7 km with a depth of 27.1 km. From here there is a sharp increase in depth to 30.2 km over a distance of only 8.9 km, modelled by OBS 308 (Fig 4.9) The depth then continues to increase gradually towards the south-eastern end of the profile, ending up at 31.2 km.

- Two floating reflectors were introduced between the intra-crustal layer and the Moho, and are modelled by OBS 301 (Fig 4.2) and OBS 307 (Fig 4.8). Another floating reflector is introduced within the upper mantle in order to model arrivals on OBS 301 (Fig 4.2) and OBS 303 (Fig 4.4). All these reflectors point to a general westwards dipping trend within the basement and upper mantle.
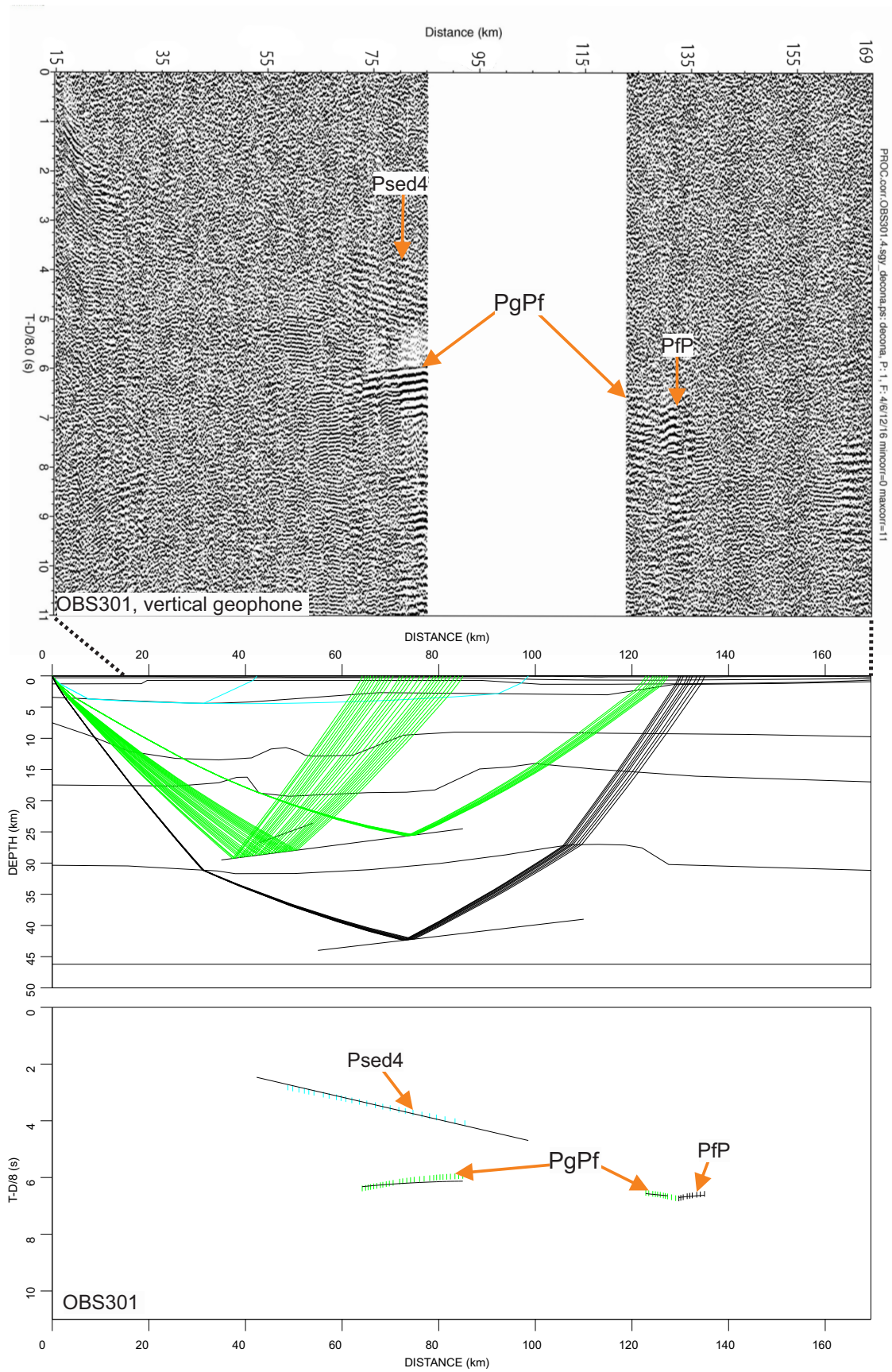
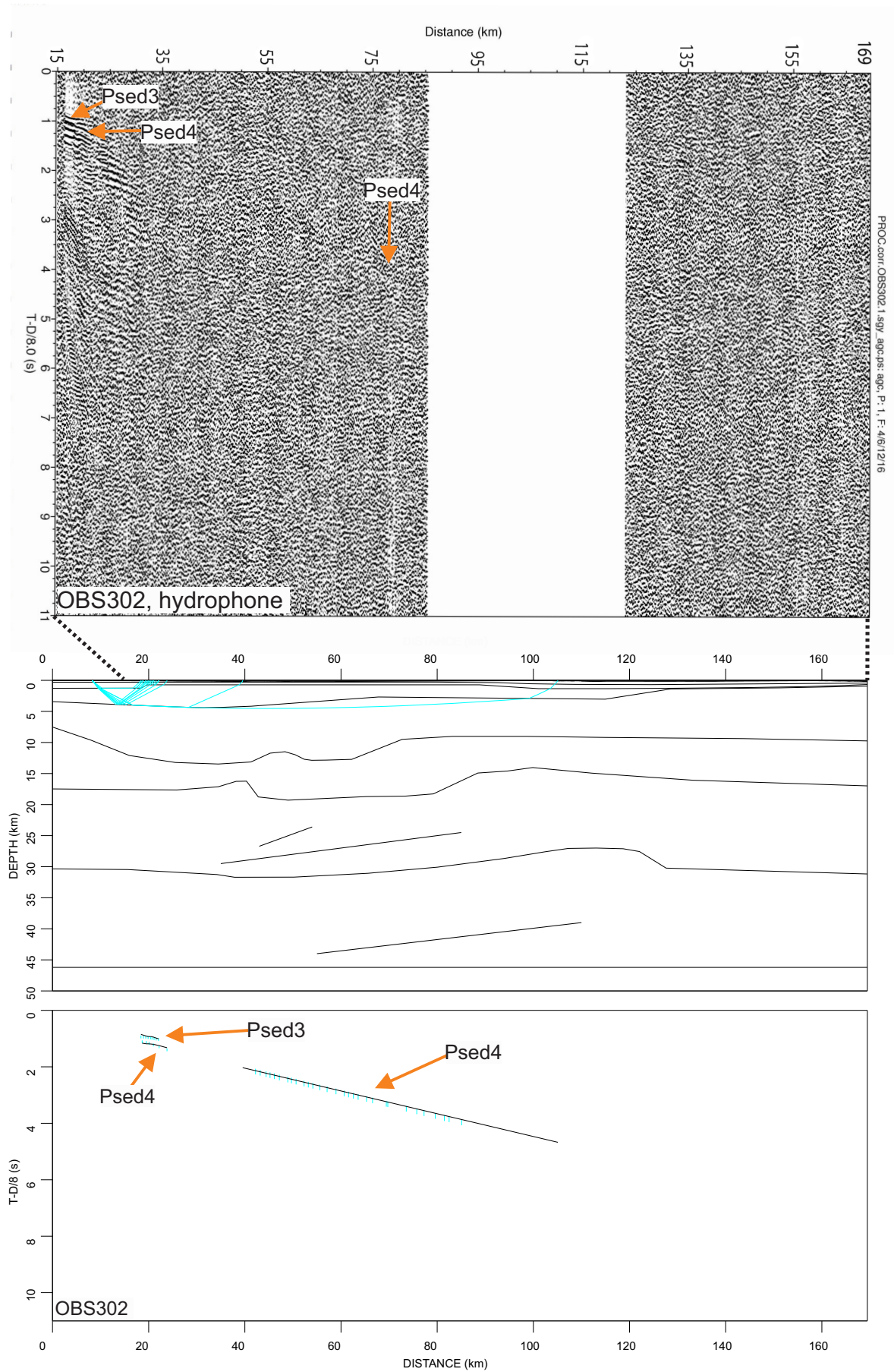**Figure 4.2:** *Interpreted phases on seismogram, raypaths through the model and modelled phases of OBS 301.*

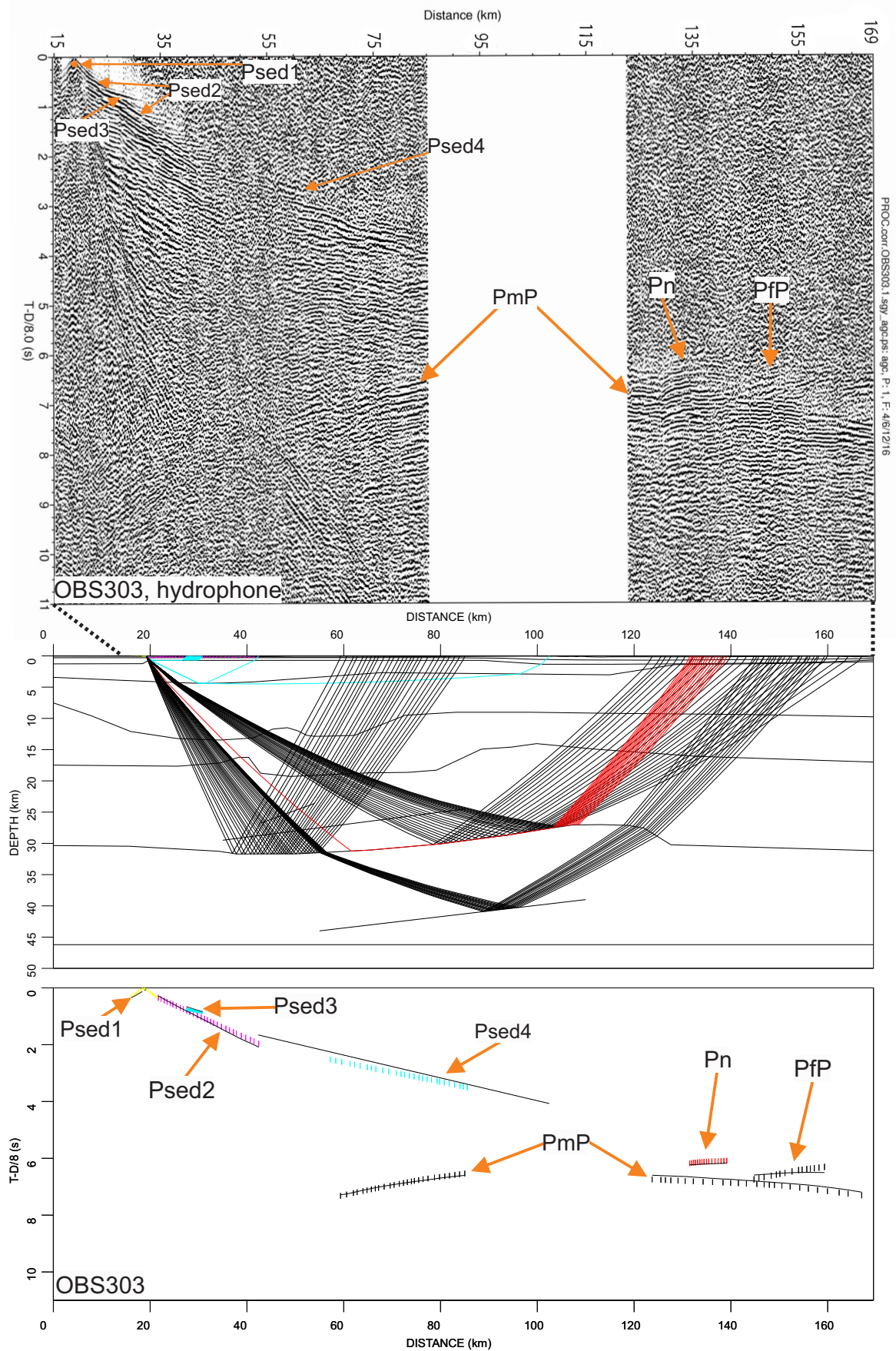**Figure 4.3:** *Interpreted phases on seismogram, raypaths through the model and modelled phases of OBS 302.*

Figure 4.4: *Interpreted phases on seismogram, raypaths through the model and modelled phases of OBS 303.*

Figure 4.5: *Interpreted phases on seismogram, raypaths through the model and modelled phases of OBS 304.*

Figure 4.6: *Interpreted phases on seismogram, raypaths through the model and modelled phases of OBS 305.*
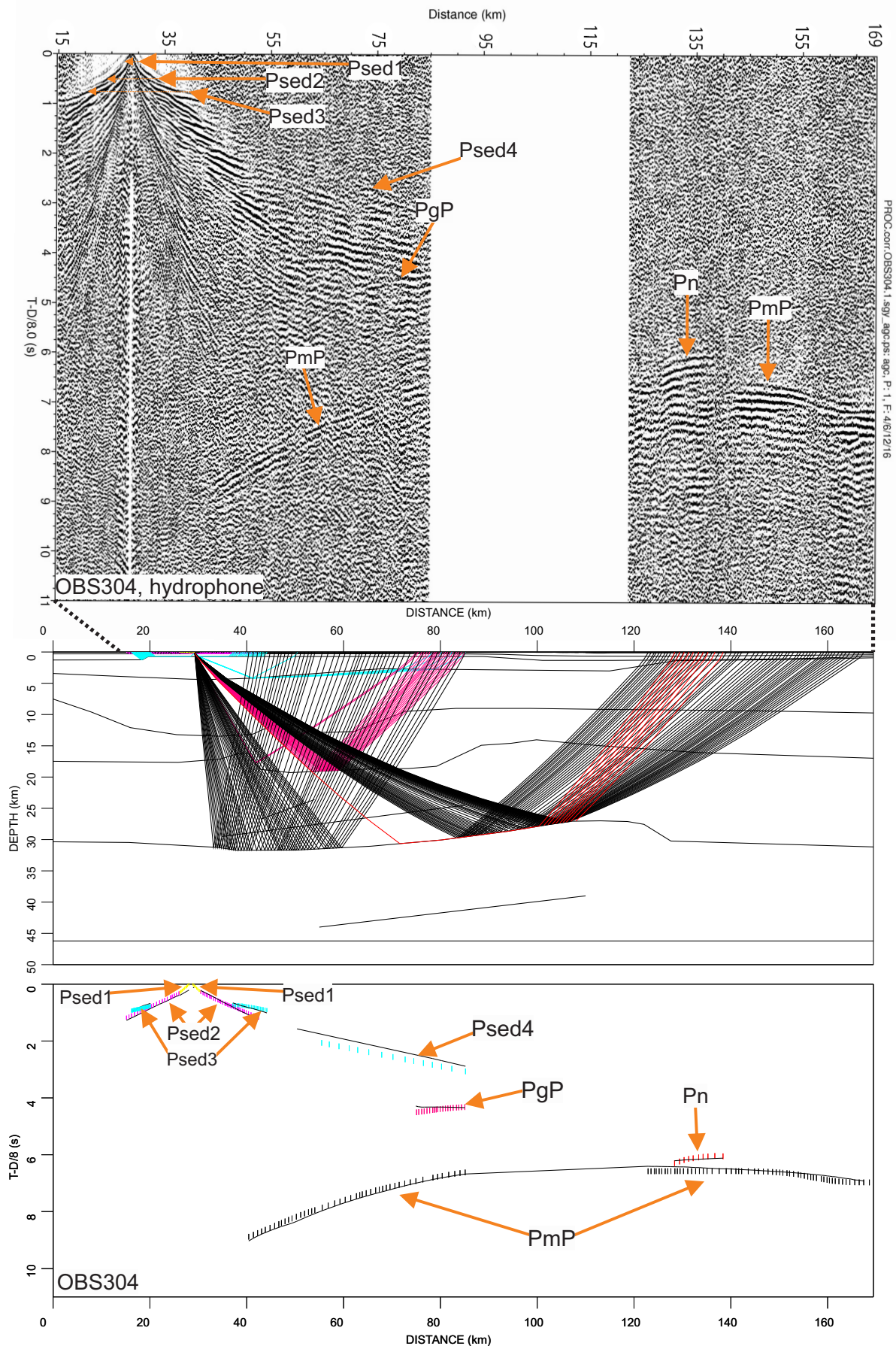
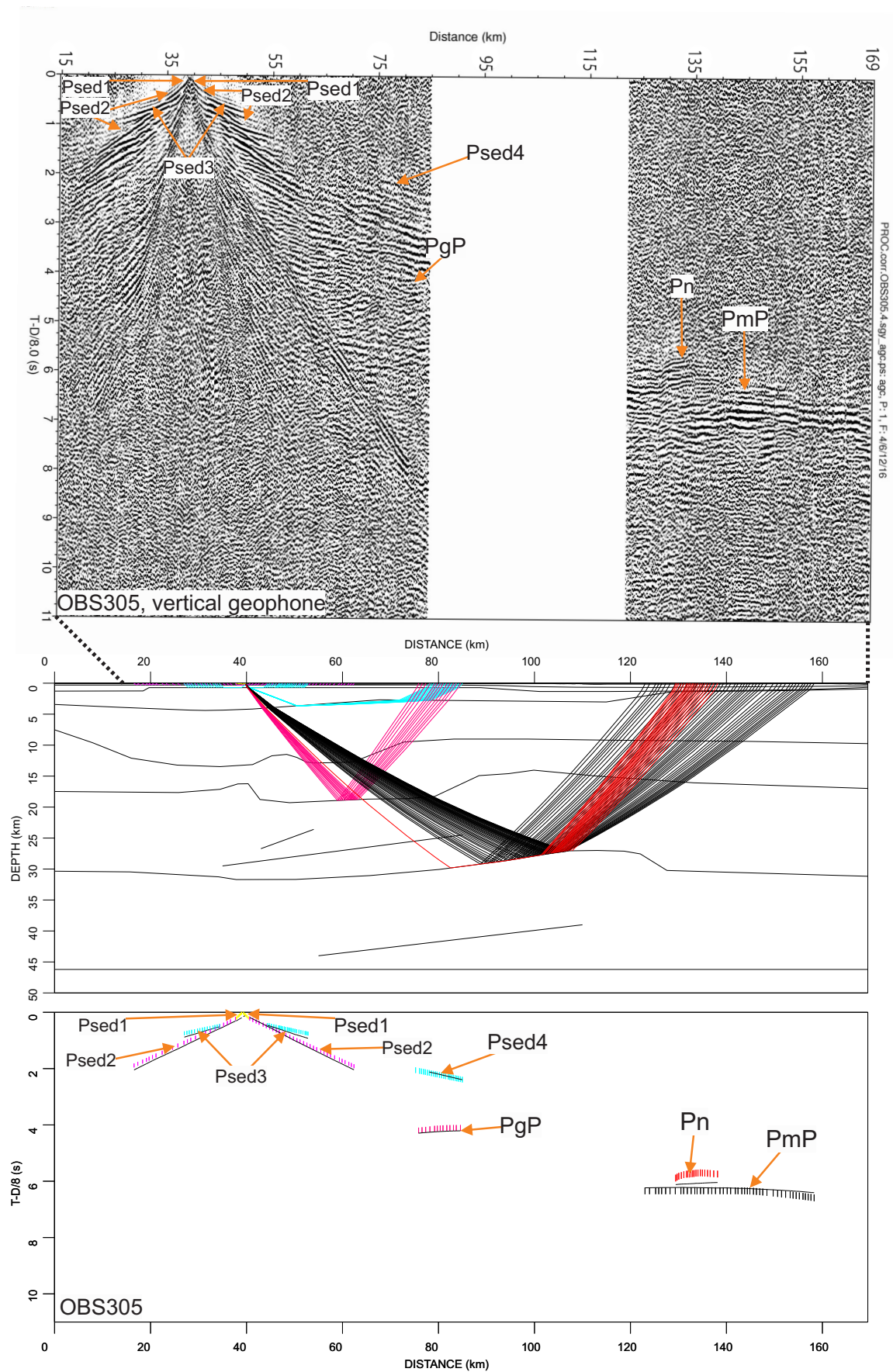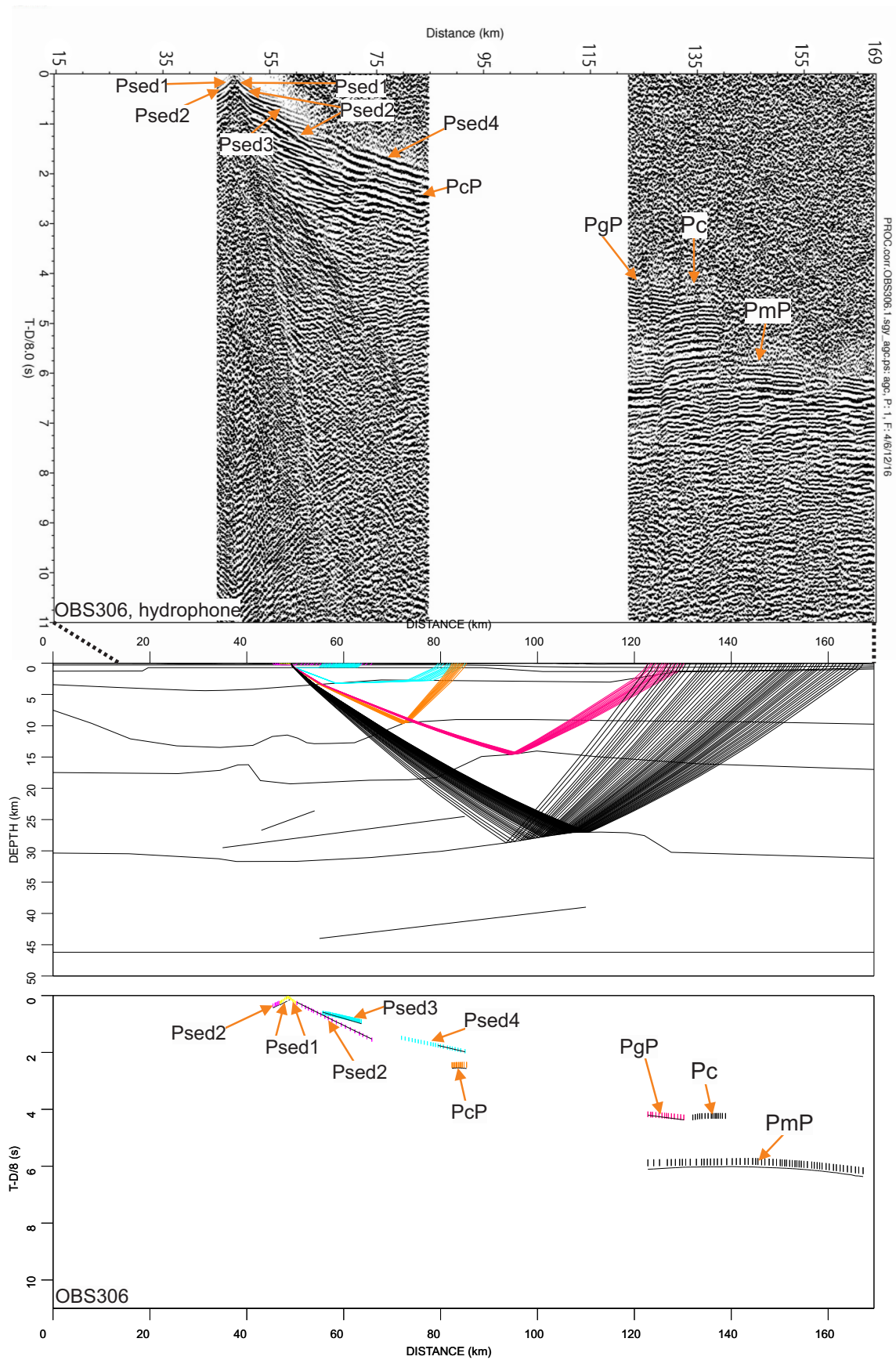**Figure 4.7:** *Interpreted phases on seismogram, raypaths through the model and modelled phases of OBS 306. Pc-phase was not modelled.*
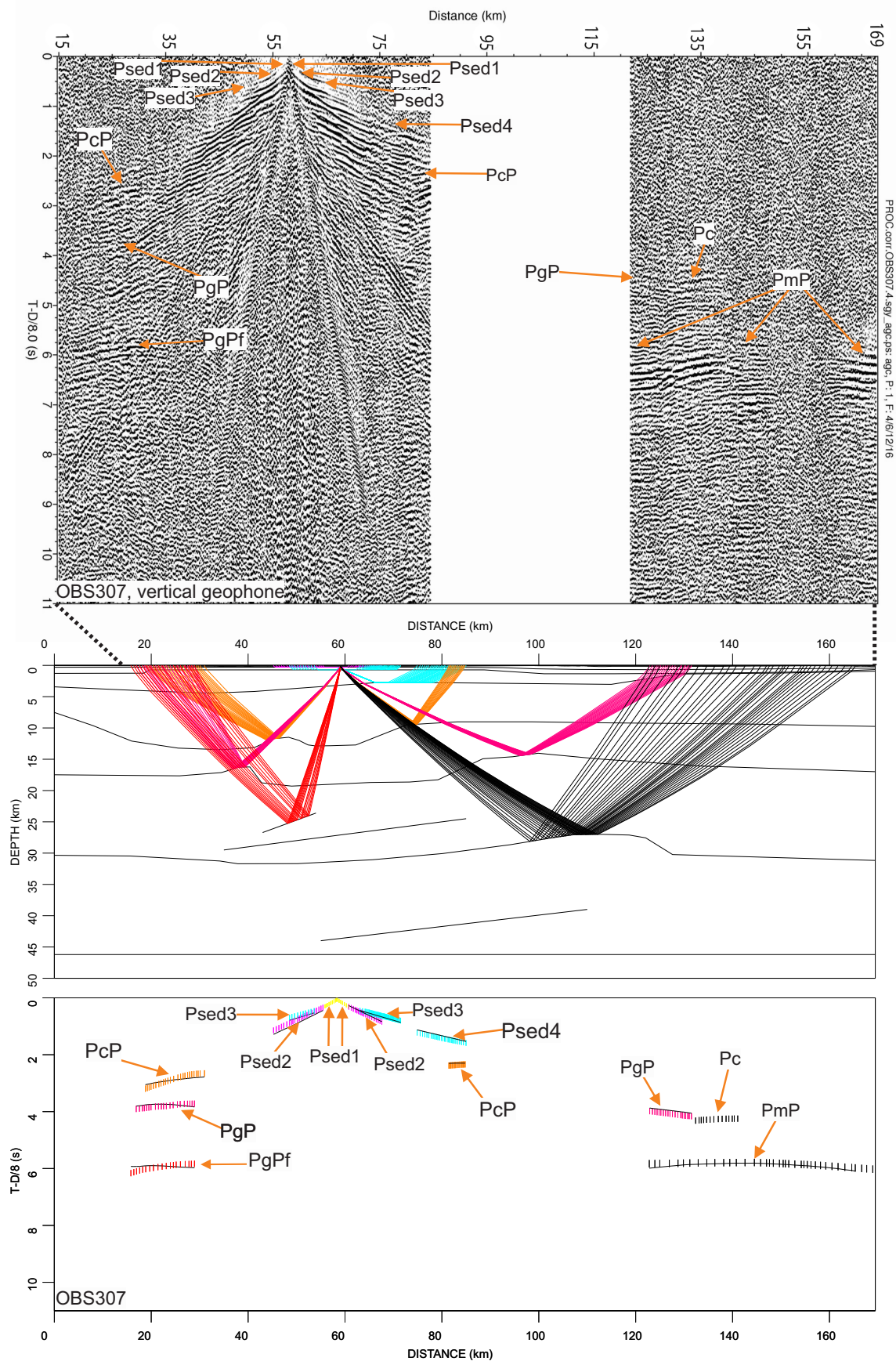
Figure 4.8: *Interpreted phases on seismogram, raypaths through the model and modelled phases of OBS 307. Pc-phase was not modelled.*
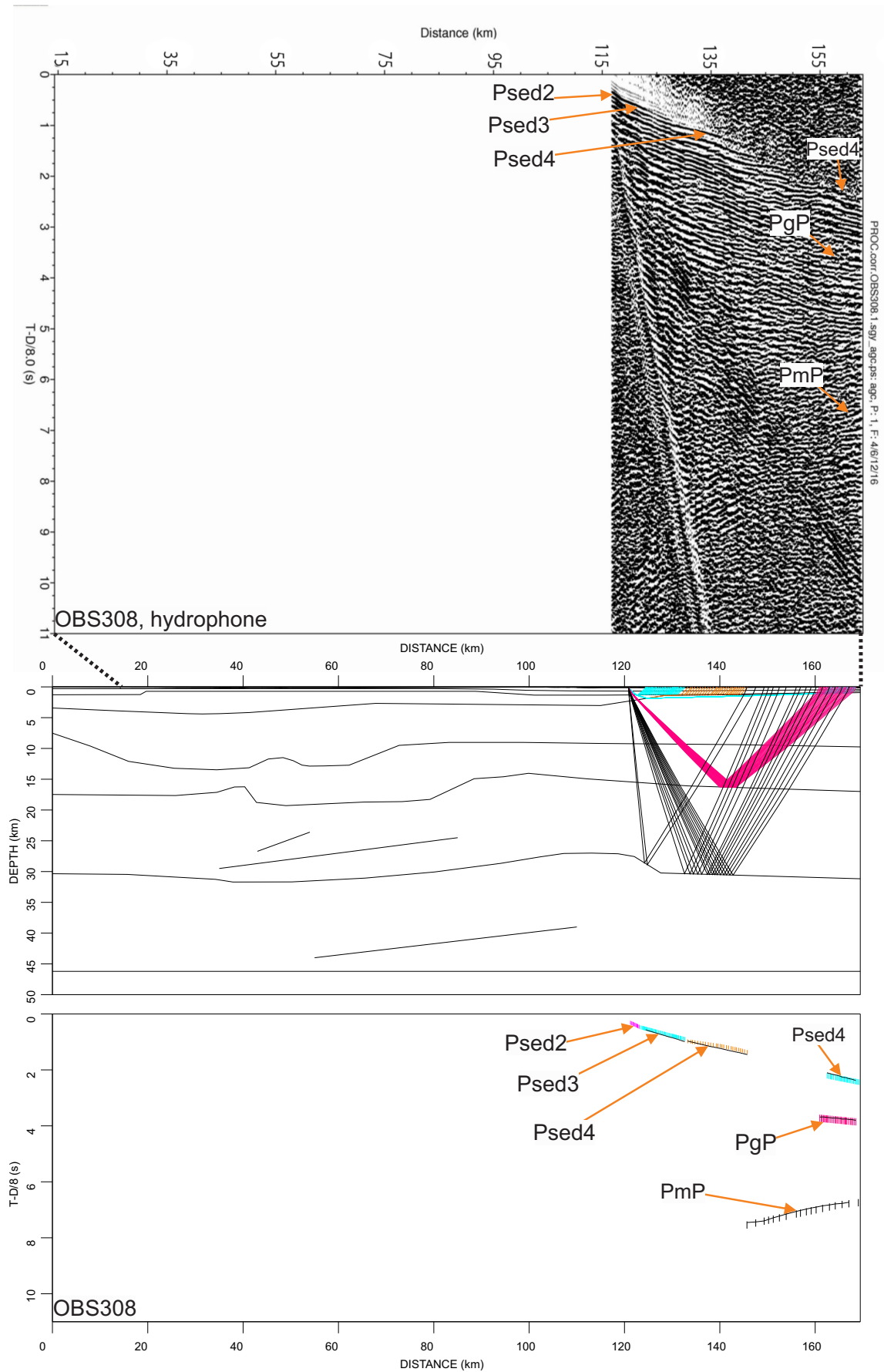
Figure 4.9: *Interpreted phases on seismogram, raypaths through the model and modelled phases of OBS 308.*

4.2 Uncertainties

Results from OBS-modelling are non-unique, and no additional types of data, such as MCS, gravimetric and magnetic data were included in this thesis. In addition to this, because of shallow water depth, there was an area from ca. 85 km to ca. 122 km where the airguns did not fire at all, leaving an area of the same length with no data on all of the seismograms. In addition, OBS 306 (Fig 4.7) lacked data from 15-45 km, and OBS 308 (Fig 4.9) from 15-118 km on the seismograms. This resulted in several fairly short interpretations of uncertain dip leading to larger uncertainties.

The gap in data towards the middle of each seismogram hindered the ability to trace many of the interpretations with as large offset as would have been desirable, and as a result the raycover of the final model suffered in a corridor of the same width as the gap, dipping about 40 degrees to the north-west (Fig 4.10).
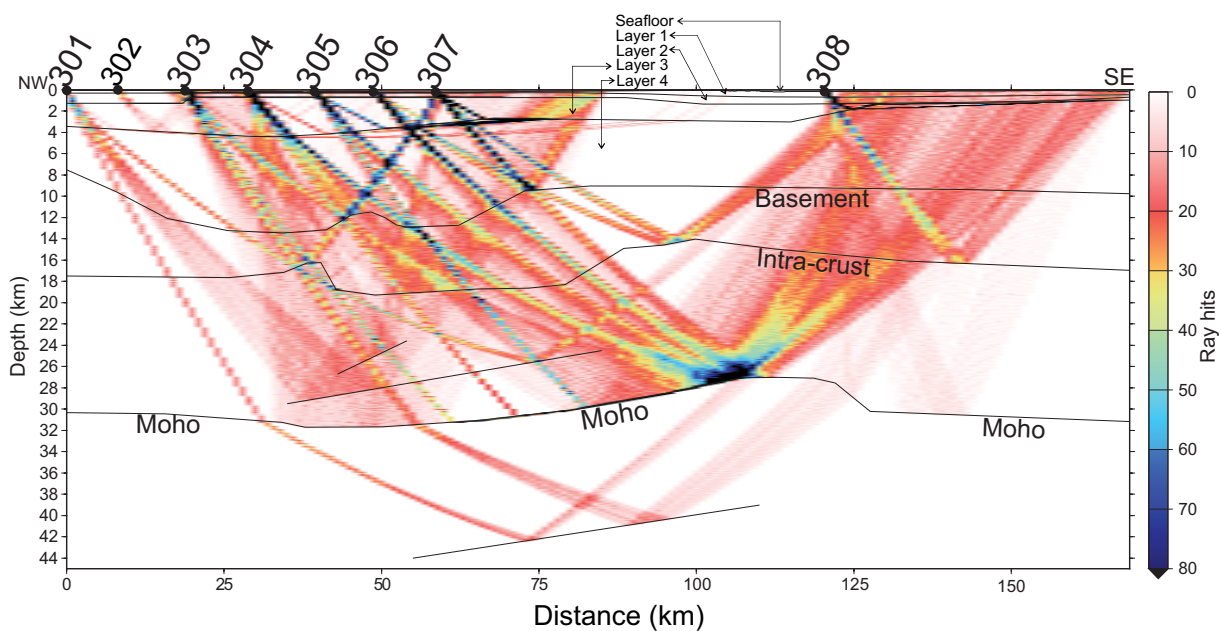

Figure 4.10: *Display of the number of ray-hits throughout the model. OBS locations along the transect displayed on top. Peak in ray-hit density near Moho top-point. Gap in ray-coverage from shot-stop clearly visible dipping towards the north-west. Top Basement and intra-crustal layers are most affected by this.*

4.2.1 Seismic model sensitivity

Rayinvr (Zelt, 1992) provides a method of comparing interpreted and calculated arrivals while making changes to the model until a reasonable fit between the two is achieved. The goal is to make a model where the travel time residuals (difference between interpreted and calculated arrival) is as small as possible, and where as many interpretations as possible are traced by the software.

Each interpretation or pick is assigned an uncertainty in time. In general, this uncertainty is set to ± one typical cycle width of the phase (Breivik et al., 2003), as it is often difficult to identify the exact onset of the arrival. Normally, the uncertainties are set to ±30 ms for the direct arrival, ±50 ms for sediment arrivals, ±75 ms for upper crystalline crust and ±100 ms for lower crust and mantle. These uncertainties, however, assume strong and clear arrivals, and weaker ones will require a higher uncertainty. It should be noted that these are general guidelines, and that the interpreted uncertainties will be subjective.

In this thesis a pick uncertainty of ±50 ms and ±70 ms was used for the upper sediment packages (Psed(x)) on most seismogram, as arrivals were reasonably clear. In some instances,±100 ms were used for the Psed5 package, as first onset of arrival and dip were harder to identify. Pg arrivals where few and short and a higher uncertainty of ±100-110 ms where given with respect to both first onset and dip.

PgP phases were relatively easy to identify on most seismograms, but did not trace with long offsets due to the gap in data, and were given uncertainties of ±100 ms were they were clear and ±110 ms were they were less clear. The phase was particularly unclear on OBS 308 (Fig 4.9), so ±130 ms was used there.

Pn phases were given an uncertainty of ±120 ms on all interpreted seismograms, as first onset was somewhat hard to distinguish. The degree of fit with modelled results was good on OBS 303 and 304, but showed a poor degree of fit on OBS 305 (Fig 4.6). PmP Phases were interpreted with clear and long offsets on most seismograms, although the first arrival of the phase became hard to pick south-east of the gap in data. A pick uncertainty of ±100 ms was given on OBS 303 and 304, and ±120-130 ms on the remaining seismograms. Rayinvr (Zelt, 1992) estimates

goodness of fit between interpreted arrivals and a model given an interpretation uncertainty through the chi-squared method, defined as:

$$\chi^2 = \frac{1}{n} \sum_{i=1}^{n} \left(\frac{T_{0_i} - T_{c_i}}{U_i} \right) \tag{4.1}$$

T_0 represents the observed arrival time, T_c the calculates arrival time, U_i the pick uncertainty and n the number of picks. The equation is weighting the mismatch between observed and calculated picks in such a way that a value of $\chi^2 \leq 1$ is considered a fit. A value closer to zero than one signifies that the model is over-parameterized. Visualizing the misfit between observed and calculated traveltimes is done easily through the root mean square (T_{rms}) equation, as it gives a measure of how far, on average, the misfit in travel time is from zero.

$$T_{rms} = \sqrt{\frac{\sum (T_{0_i} - T_{c_i})^2}{n}} \tag{4.2}$$

The variables are the same as for the χ^2 equation. The calculated values of χ^2 and T_{rms} are shown in Table 2 below. The travel time misfit is displayed in seconds.

Table 2: T_{rms} *and* χ^2 *values for The different modelled phases.*

Phase	Number of picks	T_{rms} (ms)	χ^2
Psed1	40	0.114	5.319
Psed2	206	0.078	0.959
Psed3	280	0.065	0.903
Psed4	132	0.074	1.091
PcP	51	0.094	0.791
PgP	117	0.089	0.695
PgPf	56	0.109	1.120
Pn	46	0.226	3.720
PmP	318	0.123	1.210
PfP	24	0.092	0.734
TOTAL	1262	0.102	1.526

From Table 2 it is evident that most of the modelled phases are within acceptable values for goodness of fit with the interpretations. However the χ^2 values for the Psed1 and Pn phases are significantly higher than the rest. For Psed1, this can be explained by a high shallow seismic velocity and a very thin layer, with as little as 40 meter thickness at the thinnest. This resulted in difficulties in tracing rays in the layer. As for the Pn phase, the poor fit originates from OBS 305 (Fig 4.6) where the Pn phase misses the interpretation completely. This interpretation proved hard to match with the model, as several other phases in the same area already showed a good fit. In fact, the illumination in that area is the best on the entire profile (Fig 4.10).

It was important to quantify how sensitive the model was to change of velocity and depth of the layers. In order to establish this, the velocity and depth were, independently and gradually, changed for layers in the upper and lower part of the model. The sensitivity was set to the degree of alteration at which the calculated rays no longer fit within the uncertainty bars of the interpreted ones. The sedimentary layers showed a sensitivity to change in depth larger than $\pm$ 0.35 km and change in velocity larger than $\pm$ 0.2 km/s. The middle part of the model showed sensitivities of around $\pm$ 0.35 km in depth and $\pm$ 0.13 km/s in velocity, while the Moho had a sensitivity to change in depth of $\pm$ 0.7 km and change in velocity of $\pm$ 0.1 km/s.

5 Discussion

5.1 Correlation to surrounding profiles

5.1.1 Sedimentary P-wave velocities and stratigraphy

High P-wave velocities of 4.5 km/s were found just beneath the seafloor (Fig 4.1). This velocity remains the same to the bottom of the first layer in the eastern part of the profile but increase to 4.55 km/s in the western part. The next two layers both show a general trend of increasing seismic velocities from west to east. These velocities are attributed to higher consolidation of the sediments at larger burial depths before extensive erosion during the Late Cenozoic Pliocene-Pleistocene period (Vorren et al., 1990; Richardsen et al., 1993; Sættem et al., 1994; Dimakis et al., 1998; Grogan et al., 1999).

On Edgeøya, to the north-eastern part of the profile, there are outcrops of Triassic and Cretaceous age, while Cretaceous outcrops are found on Spitsbergen to the west of the profile (Fig 2.1). Breivik et al. (2005) points out that the extent of denudation have been greater on Spitsbergen than on Edgeøya. The model in this thesis is also in accordance with this, displaying velocities of 6 km/s at depths as shallow as 1.1 km in the south-eastern part of the profile and 4.5 km depth at its deepest in the north-western part.

5.1.2 Basement

The upper basement shows a velocity increase from 6.05 km/s in the south-eastern end to 6.11 km/s in the range 19-58 km along the profile. The velocity then decreases to 6.05 km/s in the north-western end. High velocities in the lower sediments increase from 6 km/s in the south-eastern end to 6.10 km/s in the north-western end. These are moving into the realm of typical crystalline velocities, and leads to a low seismic impedance contrast to the basement.

Both magmatic intrusions and carbonates are able to produce these high velocities. There is a history of Early Cretaceous magmatism in the region (Grogan et al., 2000; Polteau et al., 2016; Minakov et al., 2012), and Krysiński et al. (2013) have

identified Lower Crustal Bodies (LCB) at depths of 20-30 km beneath Sørkapp and east of Edgeøya. Assuming the pick for basement is correct, the overlying packages (sedimentary layers 4 and 3) would be of Devonian to Permian age, known to have produced huge carbonate beds (Worsley, 2008). Considering the large scale and uniformity of the modelled high velocities, it seems more likely that they are caused by Late Devonian-Early Permian carbonates.

The profile in this thesis (Profile 3) does not overlap directly with any other OBS profiles, but it does come close, within 20 km, of profiles 1,2 and 10 of Breivik et al. (2005) (Fig 1.1). However, the nearest point of the profiles to Profile 3 is at their very end, where there is a lack of illumination on all three. In addition, the MCS lines that the initial models for the three profiles are based upon, have an uncertain constraint on the basement and no constraint at all for the Moho. This means that any close to direct tying of the Moho between profiles 1, 2 and 10 to Profile 3 is not feasible.

Breivik et al. (2005) created a depth grid to basement and Moho (Fig 5.1) through a triangulation of the OBS profiles 1, 2, 10 and 3e in order to visualise the depth-to-Moho and depth-to-basement. About halfway between Profile 10 and Profile 3e further constraint is given by the MCS profile SVA-2 (Eiken, 1994). Inserting Profile 3 into the grid gives an opportunity to compare the modelled basement and Moho depths to the previously estimated levels in the area.

In terms of correlation of the basement to the interpolated depth-grid, the geometry of the north-western part of the profile fits well. The grid in that area is mainly influenced by Profile 10 (Fig 5.3) (Breivik et al., 2005), so a comparison of that profile to Profile 3 (Fig 4.1) gives a more detailed picture of any differences than comparing to the depth-grid alone.

There are two large basins in the north-western part of the Profile 3 separated by a structural high in between, all of which are seen also in Profile 10. The depth is larger on Profile 3 (Fig 4.1), by about 3.5 km in the western basin, 2 km in the eastern basin and 5.5 km on the high in-between them. As for the eastern basin, the reduced depth is in accordance with the proposed depth-grid (Fig 5.1), showing a shallowing of the basin before its termination to the south of Profile 3. The

discrepancy between the high and eastern basin can be explained by taking into account the lacking illumination of the top basement in both Profile 3 (Fig 4.10) and Profile 10 (Breivik et al., 2005). As for the general geometry, this model lends itself to the proposition of Breivik et al. (2005), that the western basin and adjacent high are continuations of those found in Profile 3e/IKU-D (Fig 5.3) by Breivik et al. (2003). South-west of 83 km, there is no illumination of the basement, and all information of basement depth and velocity come from rays travelling through from underlying layers. The shallowest point in this area is 9 km compared to 6-7 km in the grid, and deepens very gradually to 9.8 km at the south-western end of the profile. This is close to the modelled depth of 10 km of Profile 2 in that area (Breivik et al., 2005).
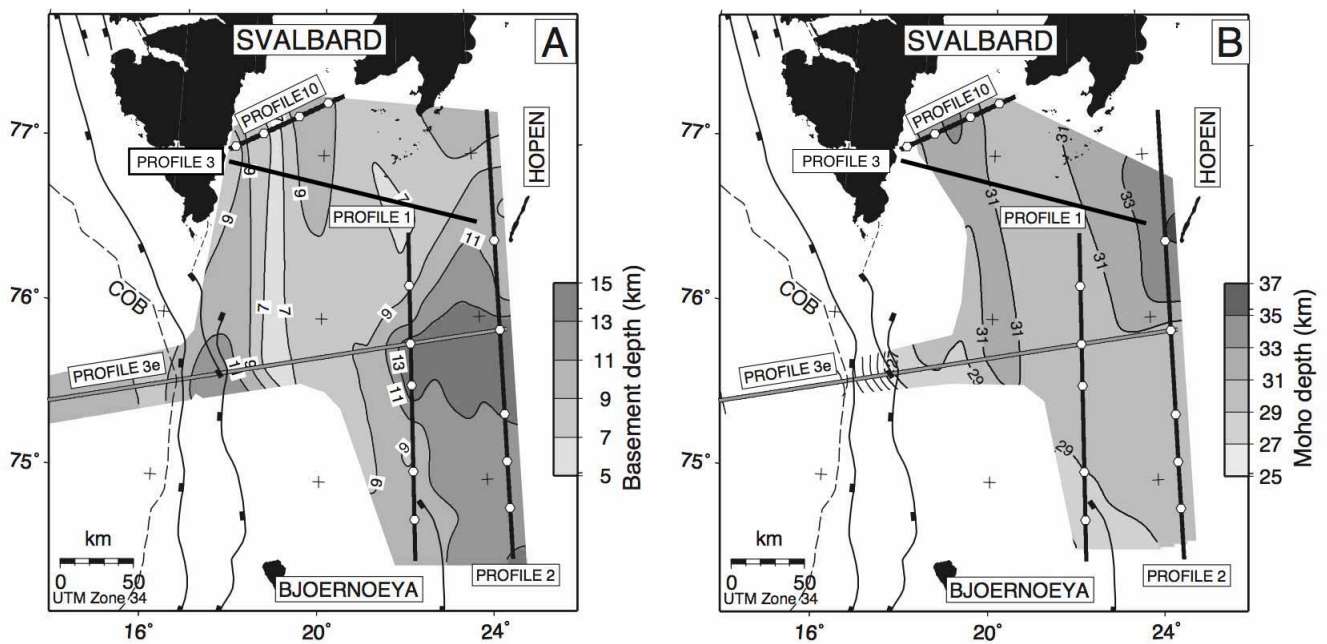

Figure 5.1: *A: Contoured basement depth based on OBS modelling of profiles 1,2, 3e and 10. B: Contoured Moho depth based on OBS modelling of profiles 1,2,3e and 10. Profile 3 is the subject of this thesis. Figure modified from Breivik et al. (2005).*

5.1.3 Moho

Comparing the depth-to-Moho for the Profile 3 model and the depth-grid, shows a general accordance with respect to the geometry of the two. Accounting for the

lack of detail provided by the depth-grid, the north-western part of Profile 3 fits reasonably well, showing a depth of 31 km about one third of the way along the profile, and rising to both sides. This 31 km depth coincides well with the crustal root observed on Profile 3e and Profile 10 in Breivik et al. (2005) as well as Krysiński et al. (2013), offering further justification for the large interpolation distance when constructing the grid. That being said, the structure is less distinguished in Profile 3 and its interpretation as a root structure more uncertain. The profile gives a shallower minimum depth that is situated further to the south-east than suggested by the grid, and a sharper deepening towards the south-eastern end.

5.1.4   Gravitational and magnetic anomaly maps

Breivik et al. (2005) introduce a free-air gravity anomaly map derived from ERS-1 and Geosat satellite altimetry measurements (Andersen and Knudsen, 1998) in combination with ship and onshore point measurements on Svalbard (Skilbrei et al., 2000) (Fig 5.2). Profile 3 is located in an area of changing gravitational anomalies. To the north-west there is a negative anomaly in the range of -10 to -25 mGal. Approximately 70-75 km along the profile in the south-east direction, the gravity anomaly shifts from negative to positive in the range of 10 to 25 mGal. In the tectonic profile (Fig 5.7) this distance seem to correlate with the two deep sedimentary basins and sandwiched structural high. The largest negative anomaly is found at the the very north-west end of the profile, where a much smaller, shallow basin is modelled. On the other hand, the basement is quickly thickening in that same area. This discrepancy can be related to high uncertainty in the model at its ends, due to lack of illumination. A slightly thinner basement and deeper Moho could result in a negative gravitational anomaly.

Gravity modelling was not done on Profile 3 as part of this thesis, but Breivik et al. (2005) performed this modelling on Profile 10 (Fig 5.2). The same basement trends are present in that profile as in the north-western part of Profile 3, as well as a small, relatively shallow (2,5 km depth) sedimentary basin. A higher than observed gravity anomaly resulted from modelling the relief of the basin, and a higher density in the basement beneath was introduced to counter this (Breivik et al., 2005). Due

to the near location of Profile 10 to Profile 3, one could assume a corresponding area of increased density in the north-western end of Profile 3. This would be expected to produce higher velocities in the north-western part of the profile, but the highest seismic velocities are in actuality found towards the middle part of the model from the bottom of the sedimentary layers and downwards. One explanation for this may be the effect of subduction erosion removing the more mafic part of the overriding plate. The increased density modelled in Profile 10 could in that case be the result of eclogites in the upper mantle as proposed by Breivik et al. (2003). While lower crustal velocities in the north-west part of Profile 3 does not really fit with the increased crustal density of Profile 10, it does seem to fit reasonably well with both the gravity and magnetic anomaly maps. In order to get a more accurate analysis, gravity modelling would have to be done on Profile 3 as well. In addition, there is a degree of uncertainty in the relationship between velocity and density, and laboratory tests show a range of densities for rocks of the same seismic velocity and visa versa (Barton, 1986).

North of Isfjorden (IF) in the density grid (Fig 5.2 (A)), there is a positive anomaly in the range of 10-20 mGal, bounded by the BFZ and Sorgfjorden Shear Zone (SSZ), corresponding to a similarly shaped and bounded magnetic anomaly seen in (Fig 5.2 (B)). The trend and magnitude of this anomaly is again similar to a double anomaly seen further south in the grid, crossing the north-western end of Profile 3. In the same area there seem to be a more diffusely defined negative gravity anomaly.

Moving south-east along Profile 3, there is a transition from negative to positive gravity anomalies, appearing smooth and stretching over a wide area encompassing the Island of Hopen and Edgeøya (Fig 5.2 (A)). This coincides reasonably well with a decrease in Moho and basement depth, and corresponding thinning of the lower density overlying sediment packages in the Profile 3 model (Fig 5.7). In the same area as the negative-positive gravity anomaly transition, there is a positive magnetic anomaly that encompasses the remainder of the profile in the south-east direction. The front of this anomaly seems to follow the trend of the supposed continuation of the BFZ, and further south-east we encounter a similar anomaly in the eastern

part of Profile 3e (Fig 5.2 (B). Breivik et al. (2005) interprets this as a transition from intermediate to more felsic basement, coincident with the supposed suture and transition from Barentsia to the east and Laurentia to the west. This point will be elaborated in the next section.
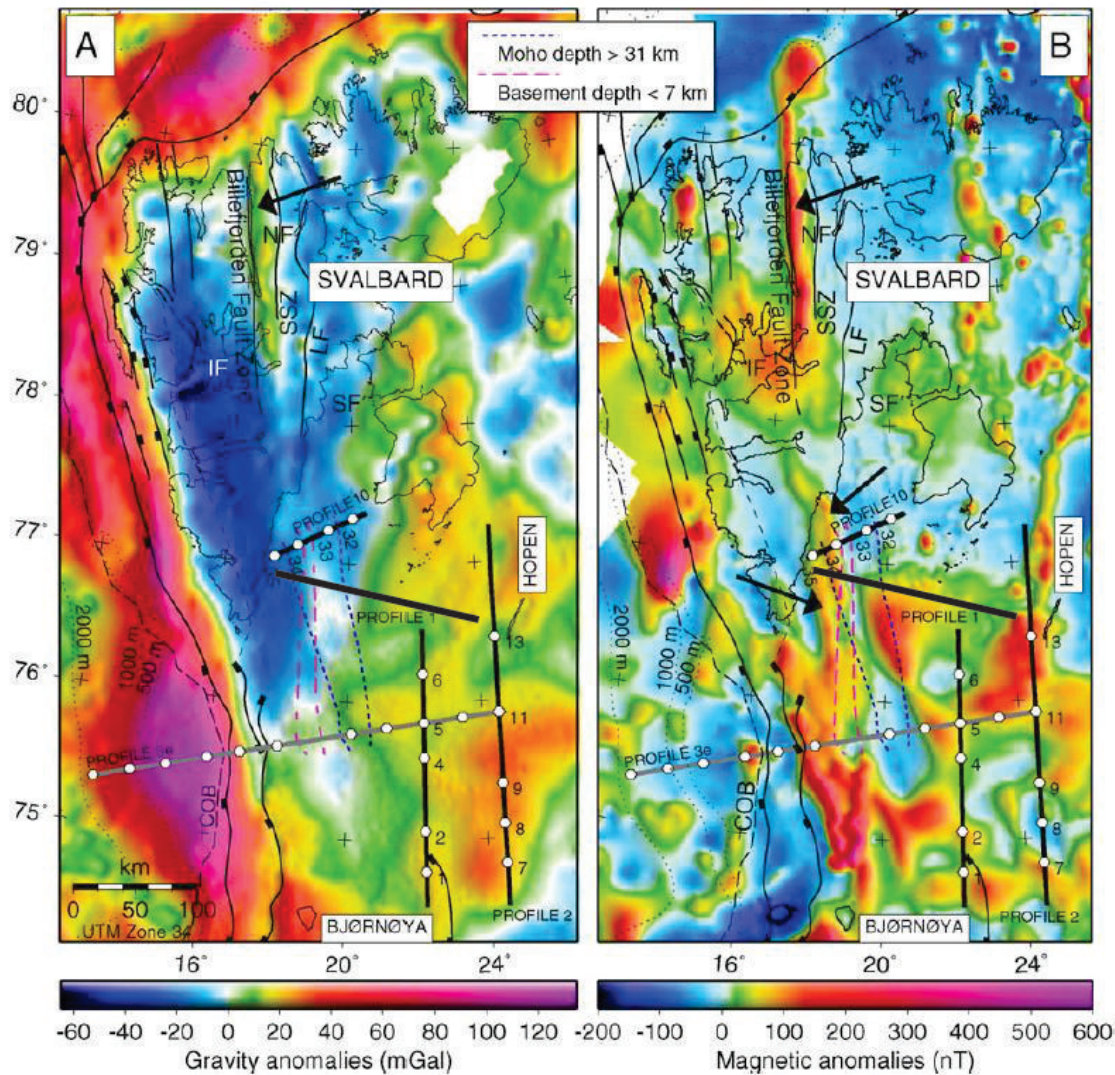

Figure 5.2: *A: Composite ERS-1 satellite and land measurements gravity map with survey navigation (Skilbrei et al., 2000). Land gravity is Bouger reduced, marine is Free Air. B: Magnetic anomaly map from surface and airborne measurements (Olesen et al., 1997). LF: Lomfjorden Fault, NF: Ny Friesland, IF: Isfjorden, SF: Storfjorden, SSZ: Sorgfjorden Shear Zone (Manby, 1990). Figure modified from (Breivik et al., 2005)*
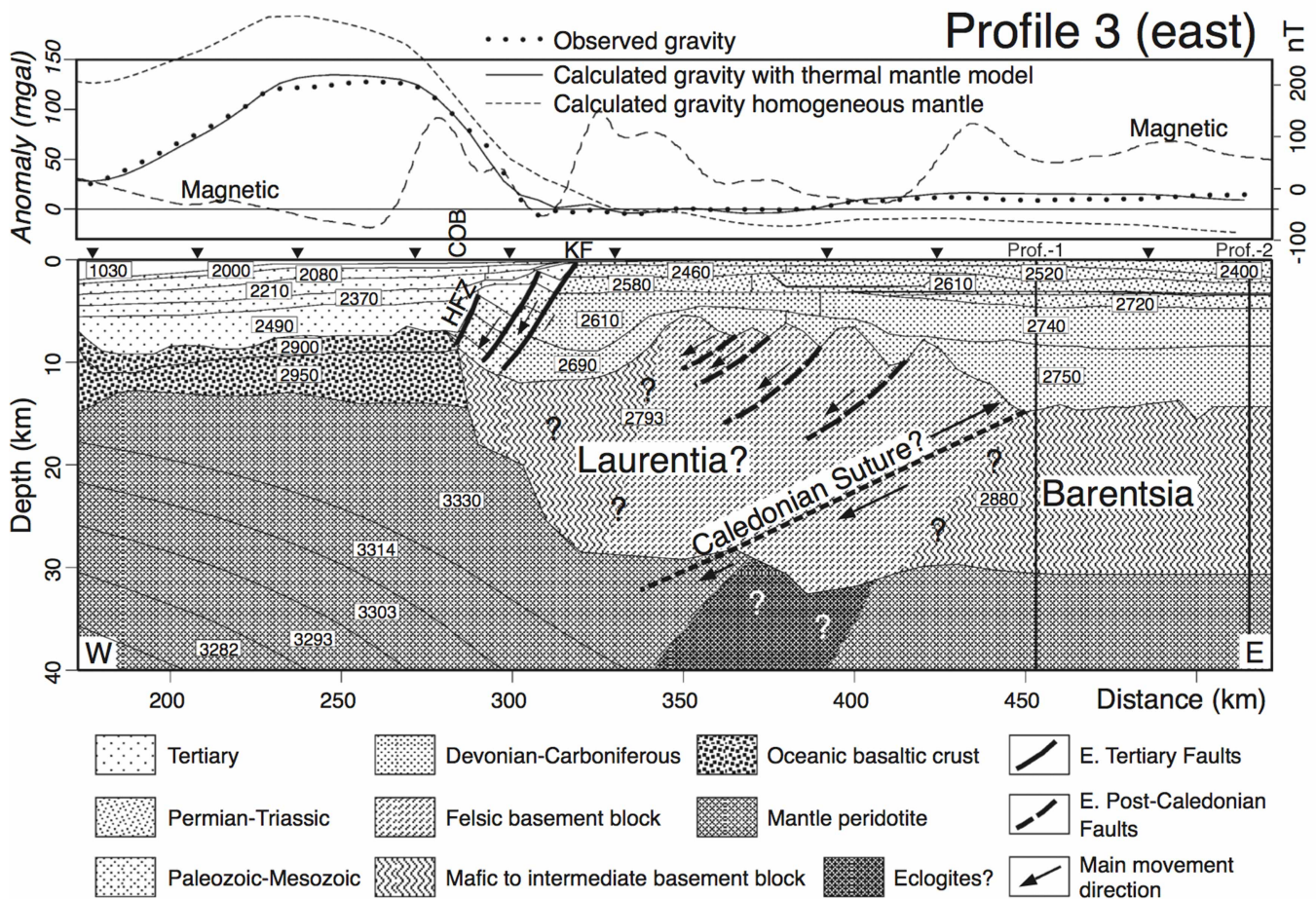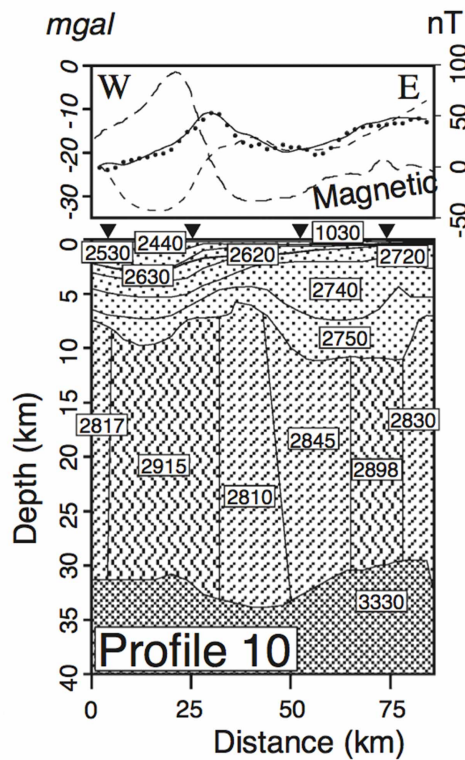
Figure 5.3: *Gravity models from Breivik et al. (2003, 2005) for Profile 10 and Profile 3e with superimposed geological interpretation.*

5.2 Caledonian suture through Svalbard

Based on interpretation of the IKU-D MCS profile (Fig 1.1), Gudlaugsson and Faleide (1994) proposed a westward dipping Caledonian suture penetrating the crust. This proposition was strongly supported by Breivik et al. (2003) based on modelling of OBS Profile 3e (Fig 1.1) coincident with the IKU-D profile, as well as gravimetric and magnetic data. One main argument in both papers is a small crustal root observed in the profiles. Further support came from Breivik et al. (2005) and Krysiński et al. (2013) through OBS Profile 10 and Horsted'05 respectively (Fig 1.1), which both showed crustal roots in the south-western part of the profiles, north of the corresponding root structures of Profile 3e/IKU-D. Aarseth et al. (2017) offers support to the Caledonide model of Gudlaugsson et al. (1998) consisting of two separate Caledonian sutures, one through Svalbard and one into the north-eastern Barents Sea through the Sentralbanken High (Fig 5.5). The Moho of the model in this thesis reaches its deepest point of 31.7 km about 38 km along the transect from the north-western end. There is a gradual shoaling to each side of the maximum depth. This is in accordance with the small crustal root observed trending northwards from Profile 3e/IKU-D to Profile 10, though due to a lack of illumination of the Moho, and thus uncertainty of any change in depth further north-west in the profile, a definite interpretation of a root structure cannot be made.

In Profile 3 (Fig 5.4), the observed double magnetic anomaly coincides with both the change from positive to negative gravity anomalies, the large Devonian basins and the proposed location of the suture zone. This reinforces a proposition made by Breivik et al. (2005) that the anomalies north of IF are the results of high grade metamorphic rock of Caledonian origin, correlating to the suture observed south of Svalbard through a trend coincident with the BFZ.

There is also a general westwards-dipping structural trend in the crust and mantle, indicated by the position of floating reflectors, as well as top basement and the intra-crustal layer. Further west to the very end of the profile there is a thickening of the basement, and possible signs of thrusting indicated by the position where the suture intersects the intra-crustal layer and top basement (Fig 5.4). This sup-

ports the hypothesis of a westward dipping Caledonian suture and subduction zone in the area. The constraint on top-basement in the model is very poor compared to the intra-crustal layer, so a larger emphasis is placed on the intra-crust when determining a possible position of the suture.
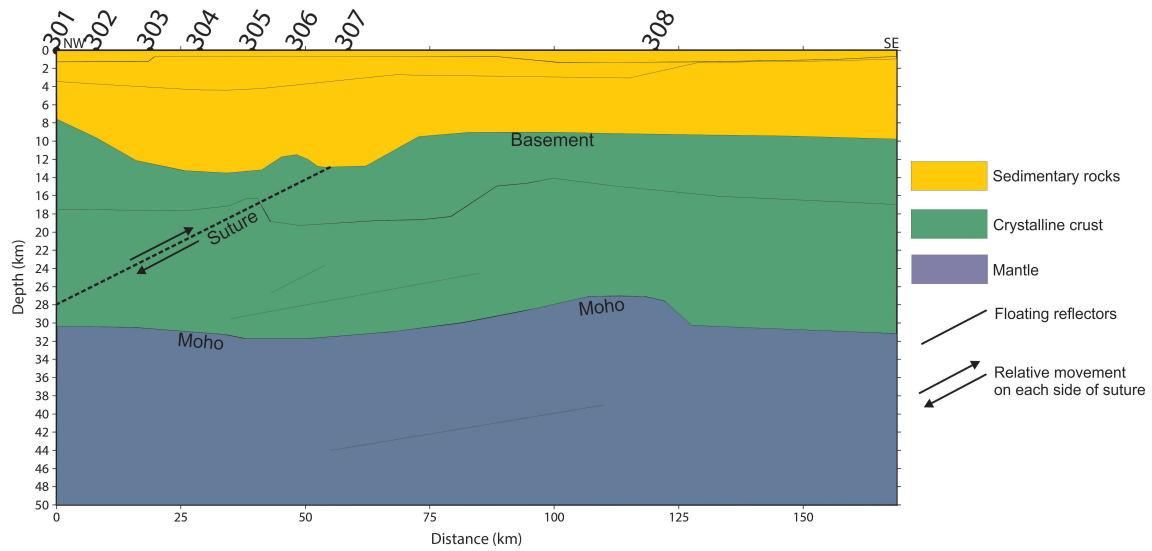

Figure 5.4: *Location of suture in tectonic model of Profile 3.*
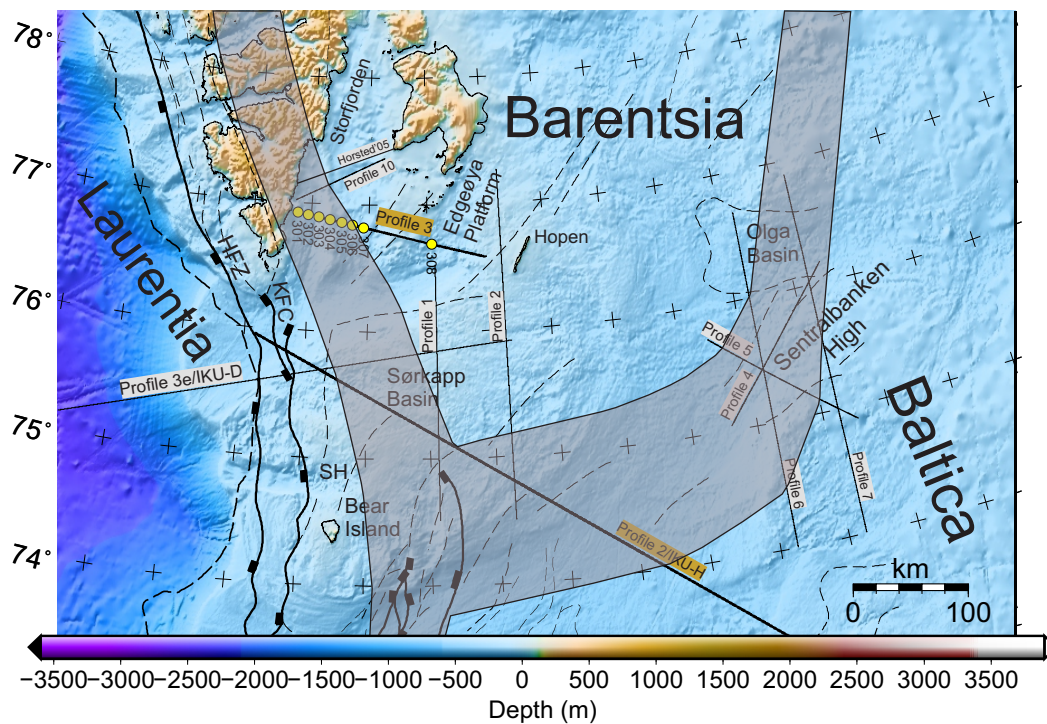
Figure 5.5: *Location of Profile 3 together with location of proposed Caledonian Suture zones. The location is based on a Caledonide model by (Gudlaugsson et al., 1998) and modelled OBS profiles by (Breivik et al., 2002, 2003, 2005; Krysiński et al., 2013; Clark et al., 2013; Aarseth et al., 2017) as well as Profile 3. The suture cuts basement and Moho at the edges of the grey area.*

5.3 Correlation to recent seismic activity

Starting in February 2008 with an earthquake of magnitude M_ω 6.1, a sequence of more than 2000 earthquakes have occurred in Storfjorden south of Svalbard. The north-easternmost extension of this sequence is marked by a magnitude M_ω 5.2 earthquake close to Edgeøya on 29 March 2016 (Tjåland, 2017) (Fig 5.6). This sequence of earthquakes have been the subject of several articles (Pirli et al., 2010, 2013; Junek et al., 2013, 2015; Ottemöller et al., 2014), as well as a recent master's thesis by Tjåland (2017) focusing on relocation of the events. Findings range from NE-SW trending strike-slip, to oblique normal faults, and possible NW-SE trending oblique normal faults assosiated with pull-apart structures. The epicenters of the earthquake cluster occur along a ENE-WSW strike, passing probable southern extensions of the BFZ and SFZ (Ottemöller et al., 2014).

Bergh and Grogan (2003) have suggested the development of a Tertiary dextral shear zone running NE-SW through Storfjorden during the formation of the WSFTB. Pirli et al. (2013) interprets the earthquake sequence as a NE-SW striking, dextral oblique normal fault, dipping steeply SSE, an interpretation that is supported by Tjåland (2017) and Ottemöller et al. (2014), and are proposed to represent a NE-SW oriented strike-slip fault system accompanied by intermediate oblique normal faults.

Ridge structures are observed in the eastern ends of both Profile 10 (Fig 5.3, 5.6) (Breivik et al., 2005) and Horsted'05 (Czuba et al., 2008) (also part of Krysiński et al. (2013)), at depths of 2-4 km and 4-5 km respectively. Piepjohn et al. (2013) proposes that these may hold a NE-SW trend coincident with that of the earthquake sequence, and Faleide et al. (1984) identifies a ridge bounded by two normal faults south of the profiles (Fig 5.6).
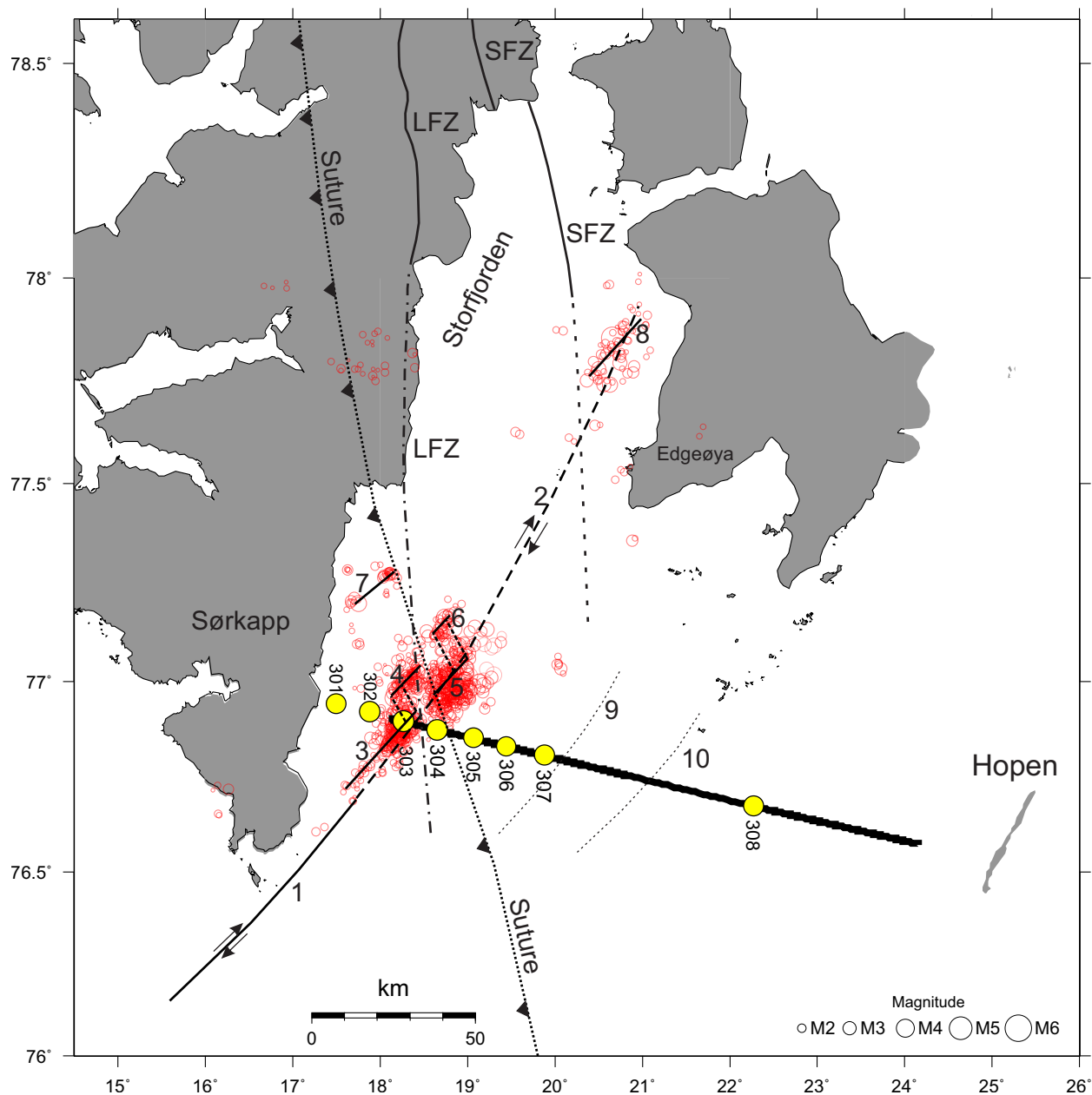
Figure 5.6: *Location of Profile 3 with OBS positions marked in yellow, in relation to recent earthquakes relocated by Tjåland (2017). The size of the circles represent magnitude of the earthquakes. 1: Assumed Tertiary shear zone from Bergh and Grogan (2003), 2: Interpreted continuation of the shear zone into Storfjorden (dashed line). 3-8: NE-SW oriented strike-slip faults (Ottemöller et al., 2014; Tjåland, 2017). Faults 3-6 are accompanied with pull-apart structures (dashed lines). 9-10: NE-SW trending ridge bounded by normal faults (Faleide et al., 1984). SFZ: Storfjorden Fault Zone with inferred continuation (dashed line) by Dallmann (2015). LFZ: Lomfjorden with inferred continuation (dashed line) by Dallmann (2015). The suture-line is placed where the suture cuts top-basement and follows one interpretation of the BFZ (e.g. Ohta, 1982; Steel and Worsley, 1984).*

Identifying correlating structures in Profile 3 represents a challenge due to the lack of illumination in the area. There is a change in basement depth from $\sim$ 12 km to $\sim$ 9 km moving eastwards along the profile at about 70 km, accompanied by a similar change in the underlying intra-crustal layer, which may represent a southern continuation of the ridge structures further north. In addition, a possible presence of one or more large faults in the area are implied by hindrances to seismic signal propagation somewhere in the south-east part of the profile, indicated by the abrupt cut-off of seismic phases from the crust and mantle recorded on several OBS's (e.g. OBS 301 (4.2), OBS 307 (4.8)). Should this be the case, the trend of the ridge structures matches that of the earthquake sequence fairly well, though they do not overlap.

The relocation of the earthquakes by Tjåland (2017) reveals at least four SW-NE trending structures, two of which are clearly visible when draping the earthquake locations over the tectonic model for Profile 3 (Fig 5.7). Both of these structures fall in an area already proposed to hold the Caledonian suture, a large decrease in basement depth to either side, as well as possible southern extensions of both the BFZ and LFZ. Furthermore, the north-eastern cluster of earthquakes nearly coincides with a possible extension of the Storfjorden Fault Zone (SFZ). In this case the clustering of earthquakes in the area could be explained by the shear zone proposed by Bergh and Grogan (2003) crossing an area of already increased structural weakness introduced by earlier events.
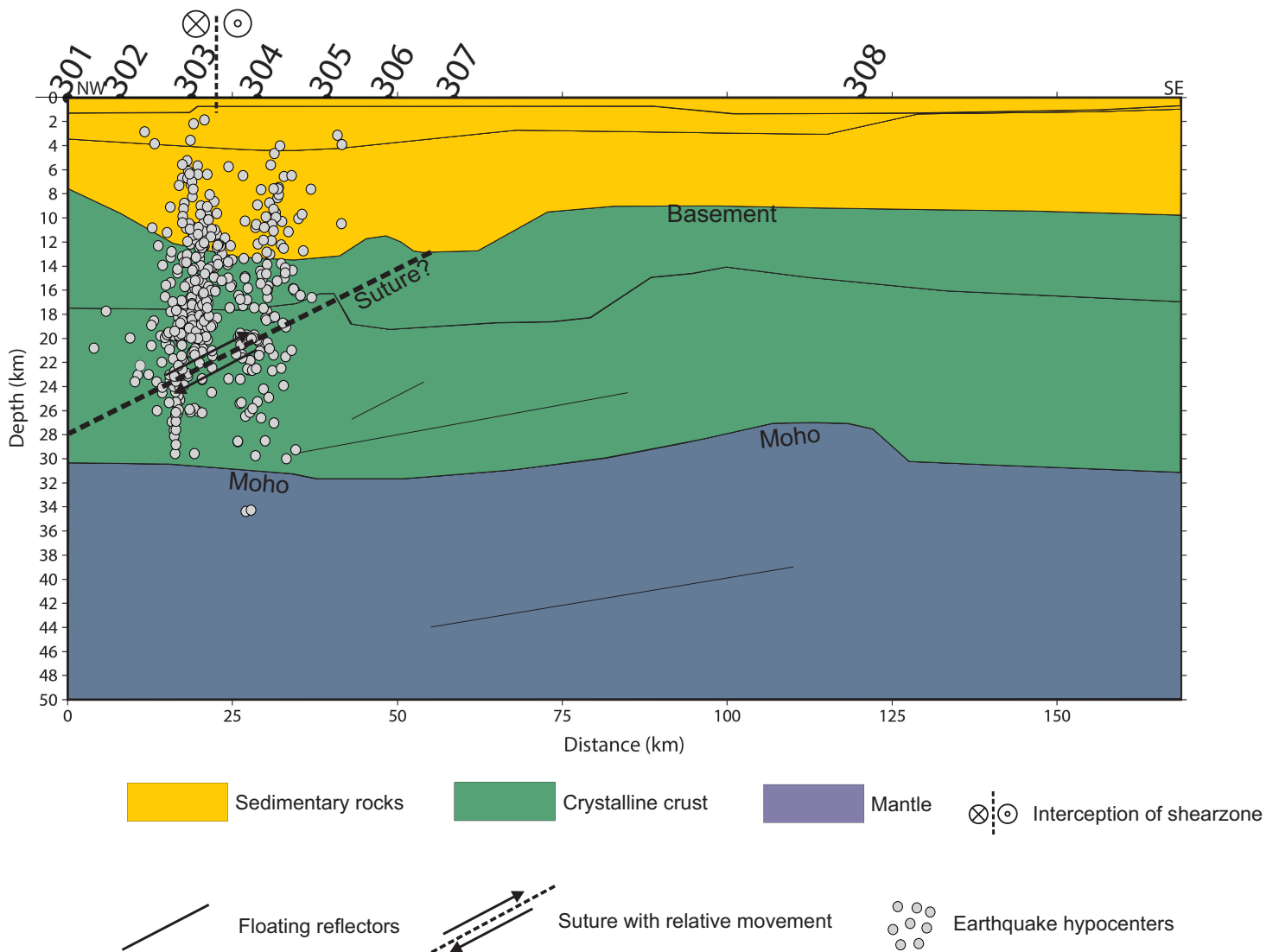
Figure 5.7: *Location of recent earthquakes relocated by Tjåland (2017) in relation to Profile 3. Hypocenters within a distance of 10 km in each orthogonal direction to the profile are included and draped over the tectonic model previously visited. Note two distinct clusters of events beneath OBS 303 and 304. Also included is the intersection of the profile and the interpreted continuation of the Tertiary shear zone proposed by Bergh and Grogan (2003). The crossed circle indicate movement away, while the dotted circle indicate movement towards.*

Several trigger mechanisms for the earthquakes have been proposed, including Early Cretaceous thermal uplift (Drachev and Saunders, 2006; Minakov et al., 2012), and present day vertical movements caused by a hot upper mantle beneath Svalbard (Klitzke et al., 2015). More local mechanisms and sources of vertical stresses like sediment loading and post-isostatic uplift may also be contributors (Fejerskov and Lindholm, 2000). However, all of these factors will generally produce vertical stresses, and does not explain the strike-slip motion. North-south extension is invoked by Ottemöller et al. (2014) in order to explain the type of faulting and stress patterns that have been found from fault plane solutions. This is backed up by Tjåland (2017), which further suggests that this type of extension is what one could expect during the early stages of rifting, and supports an earlier hypothesis by Savostin and Karasik (1981) regarding the existence of a Spitsbergen microplate (Fig 5.8). Two main models are proposed, of which one involve strike-slip movement through Spitsbergen along the Eurekan deformation front, while the other assume a larger plate boundary extending north-east and linking up with the Gakkel Ridge. While this boundary is speculative, it does fit with the NE-SW trend of the Storfjorden earthquakes as well as the lack thereof along any major N-S structures in the area.
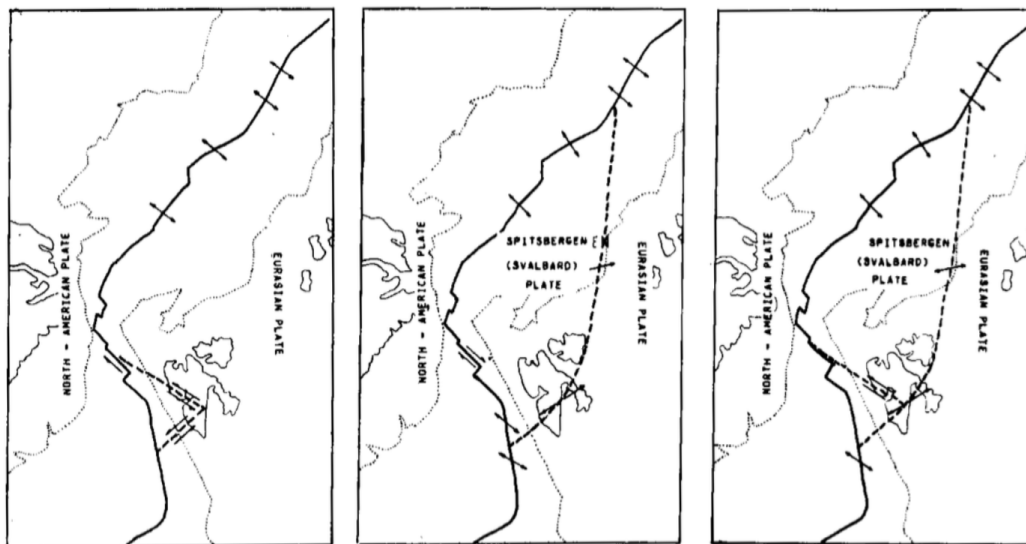
Figure 5.8: *a: A small plate bounded by the Knipovich ridge. b: a larger plate bounded by the Knipovich Ridge in the south-west and the Gakkel Ridge in the north. c: A combination of both models. Figure from Savostin and Karasik (1981).*

6 Conclusions

A 169 km long OBS profile running across Storfjorden south of Svalbard, and consisting of eight Ocean Bottom Seismometers have been obtained. Eight resulting seismograms have been processed, interpreted and modelled through forward/inverse modelling as part of the thesis. The result is a 2D P-wave velocity model of a crustal transect along the line from the seafloor to the mantle.

- While there is uncertainty regarding top basement in the model, the sedimentary layers, Moho and a intra-crustal layer are fairly well constrained.

- There are high seismic velocities present at shallow depth, attributed to regional uplift and Late Devonian-Permian carbonates, although magmatic intrusions cannot be ruled out as a contributing factor.

- This model is in accordance with the hypothesis of a suture oriented along a north-south trend through Svalbard. There is a general down-to-west dip toward the suture from the east, as well as signs of possible eastern thrusting on its western side. In addition, the deepest point of the Moho coincide with interpreted crustal roots and the proposed position of the suture from earlier work. The highest P-wave velocities are found in the middle part of the model, and can be explained by subduction erosion. Based on the trend of gravity and magnetic anomalies related to Caledonian metamorphic rock on Svalbard, the suture appears to correlate to the BFZ.

- The south-western cluster of earthquakes intersect the Caledonian suture as well as possible southwards extensions of both the Billefjorden Fault Zone and Lomfjorden Fault Zone, and resulting zones of weakness may explain the location of the cluster.

- The north-eastern cluster is located near the supposed southern extensions of the Storfjorden Fault Zone. This extension may run somewhat further east then previously assumed.

- Regional north-south extension is in accordance with earthquakes clustering around intersections of north-south oriented faults and a NE-SW shear zone, but not directly related to the major north-south oriented suture.

References

Aarseth, I., Mjelde, R., Breivik, A. J., Minakov, A., Faleide, J. I., Flueh, E. and Huismans, R. S. (2017), 'Crustal structure and evolution of the arctic caledonides: Results from controlled-source seismology', *Tectonophysics* **300**, 9–24.

Andersen, O. B. and Knudsen, P. (1998), 'Global marine gravity field from the ers-1 and geosat geodetic mission altimetry', *Journal of Geophysical Research: Oceans* **103**(C4), 8129–8137.

Barton, P. (1986), 'The relationship between seismic velocity and density in the continental crust—a useful constraint?', *Geophysical Journal International* **87**(1), 195–208.

Bergh, S. G. and Grogan, P. (2003), 'Tertiary structure of the sørkapp-hornsund region, south spitsbergen, and implications for the offshore southern extension of the fold-thrust belt.', *Norwegian Journal of Geology/Norsk Geologisk Forening* **83**(1).

Breivik, A. J., Faleide, J. I. and Gudlaugsson, S. T. (1998), 'Southwestern barents sea margin: late mesozoic sedimentary basins and crustal extension', *Tectonophysics* **293**(1), 21–44.

Breivik, A. J., Mjelde, R., Grogan, P., Shimamura, H., Murai, Y. and Nishimura, Y. (2003), 'Crustal structure and transform margin development south of svalbard based on ocean bottom seismometer data', *Tectonophysics* **369**(1), 37–70.

Breivik, A. J., Mjelde, R., Grogan, P., Shimamura, H., Murai, Y. and Nishimura, Y. (2005), 'Caledonide development offshore–onshore svalbard based on ocean bottom seismometer, conventional seismic, and potential field data', *Tectonophysics* **401**(1), 79–117.

Breivik, A. J., Mjelde, R., Grogan, P., Shimamura, H., Murai, Y., Nishimura, Y. and Kuwano, A. (2002), 'A possible caledonide arm through the barents sea imaged by obs data', *Tectonophysics* **355**(1), 67–97.

Bretel, P., Lebedeva-Ivanova, N., Meyer, O. and Minakov, A. (2014), 'Barents obs 2014: Ocean bottom survey in the barents sea'.

Clark, S. A., Faleide, J. I., Hauser, J., Ritzmann, O., Mjelde, R., Ebbing, J., Thybo, H. and Flüh, E. (2013), 'Stochastic velocity inversion of seismic reflection/refraction traveltime data for rift structure of the southwest barents sea', *Tectonophysics* **593**, 135–150.

Czuba, W., Grad, M., Guterch, A., Majdański, M., Malinowski, M., Mjelde, R., Moskalik, M., Środa, P., Wilde-Piórko, M. and Nishimura, Y. (2008), 'Seismic crustal structure along the deep transect horsted'05, svalbard', *Pol. Polar Res* **29**(3), 279–290.

Dallmann, W. K., ed. (2015), *Geoscience Atlas of Svalbard*, Rapportserie nr: 148, Norsk Polarinstitutt.

Dimakis, P., Braathen, B. I., Faleide, J. I., Elverhøi, A. and Gudlaugsson, S. T. (1998), 'Cenozoic erosion and the preglacial uplift of the svalbard–barents sea region', *Tectonophysics* **300**(1), 311–327.

Doré, A. (1991), 'The structural foundation and evolution of mesozoic seaways between europe and the arctic', *Palaeogeography, Palaeoclimatology, Palaeoecology* **87**(1-4), 441–492.

Drachev, S. and Saunders, A. (2006), The early cretaceous arctic lip: its geodynamic setting and implications for canada basin opening, *in* 'Proc. Fourth Int. Conf. on Arctic Margins, Dartmouth, Nova Scotia', Vol. 30, pp. 216–223.

Eiken, O. (1994), 'Seismic atlas of western svalbard: a selection of regional seismic transects'.

Faleide, J. I., Gudlaugsson, S. T. and Jacquart, G. (1984), 'Evolution of the western barents sea', *Marine and Petroleum Geology* **1**(2), 123–150.

Faleide, J. I., Vågnes, E. and Gudlaugsson, S. T. (1993), 'Late mesozoic-cenozoic evolution of the south-western barents sea in a regional rift-shear tectonic setting', *Marine and Petroleum Geology* **10**(3), 186–214.

Fejerskov, M. and Lindholm, C. (2000), 'Crustal stress in and around norway: an evaluation of stress-generating mechanisms', *Geological Society, London, Special Publications* **167**(1), 451–467.

Gee, D. G., Fossen, H., Henriksen, N. and Higgins, A. K. (2008), 'From the early paleozoic platforms of baltica and laurentia to the caledonide orogen of scandinavia and greenland', *Episodes* **31**(1), 44–51.

Gee, D. G. and Page, L. M. (1994), 'Caledonian terrane assembly on svalbard; new evidence from 40 ar/39 ar dating in ny friesland', *American Journal of Science* **294**(9), 1166–1186.

Gee, D. G. and Teben'kov, A. (2004), 'Svalbard: a fragment of the laurentian margin', *Geological Society, London, Memoirs* **30**(1), 191–206.

Grad, M., Mjelde, R., Czuba, W., Guterch, A., Schweitzer, J. et al. (2011), 'Modelling of seafloor multiples observed in obs data from the north atlantic-new seismic tool for oceanography?', *Polish Polar Research* **32**(4), 375–392.

Grogan, P., Nyberg, K., Fotland, B., Myklebust, R., Dahlgren, S. and Riis, F. (2000), 'Cretaceous magmatism south and east of svalbard: evidence from seismic reflection and magnetic data', *Polarforschung* **68**, 25–34.

Grogan, P., Østvedt-Ghazi, A.-M., Larssen, G., Fotland, B., Nyberg, K., Dahlgren, S. and Eidvin, T. (1999), Structural elements and petroleum geology of the norwegian sector of the northern barents sea, *in* 'Geological Society, London, Petroleum Geology Conference series', Vol. 5, Geological Society of London, pp. 247–259.

Gudlaugsson, S. and Faleide, J. (1994), 'The continental margin between spitsbergen and bjørnøya', *Seismic Atlas of Western Svalbard* **130**, 11–13.

Gudlaugsson, S., Faleide, J., Johansen, S. and Breivik, A. (1998), 'Late palaeozoic structural development of the south-western barents sea', *Marine and Petroleum Geology* **15**(1), 73–102.

Harland, W. B., Anderson, L. M., Manasrah, D., Butterfield, N. J., Challinor, A., Doubleday, P. A., Dowdeswell, E. K., Dowdeswell, J. A., Geddes, I., Kelly, S. R. et al. (1997), *The geology of Svalbard*, Geological Society.

Junek, W. N., Kværna, T., Pirli, M., Schweitzer, J., Harris, D. B., Dodge, D. A. and Woods, M. T. (2015), 'Inferring aftershock sequence properties and tectonic structure using empirical signal detectors', *Pure and Applied Geophysics* **172**(2), 359–373.

Junek, W., Roman-Nieves, J. and Woods, M. (2013), 'Tectonic implications of earthquake mechanisms in svalbard', *Geophysical Journal International* **196**(2), 1152–1161.

Klitzke, P., Faleide, J., Scheck-Wenderoth, M. and Sippel, J. (2015), 'A lithosphere-scale structural model of the barents sea and kara sea region', *Solid Earth* **6**(1), 153–172.

Krysiński, L., Grad, M., Mjelde, R., Czuba, W. and Guterch, A. (2013), 'Seismic and density structure of the lithosphere- asthenosphere system along transect knipovich ridge- spitsbergen- barents sea–geological and petrophysical implications', *Polish Polar Research* **34**(2), 111–138.

Manby, G. (1990), 'The petrology of the harkerbreen group, ny friesland, svalbard: protoliths and tectonic significance', *Geological Magazine* **127**(2), 129–146.

Minakov, A., Mjelde, R., Faleide, J. I., Flueh, E. R., Dannowski, A. and Keers, H. (2012), 'Mafic intrusions east of svalbard imaged by active-source seismic tomography', *Tectonophysics* **518**, 106–118.

Mjelde, R. (2017), Personal communication.

Ohta, Y. (1982), *Morpho-tectonic studies around Svalbard and the northernmost Atlantic*, CSPG Special Publications.

Olesen, O., Gellein, J., Håbrekke, H., Kihle, O., Skilbrei, J. and Smethurst, M. (1997), 'Magnetic anomaly map norway and adjacent ocean areas, scale 1: 3 million', *Geological Survey of Norway, Trondheim* .

Ottemöller, L., Kim, W. Y., Dallmann, W. and Waldhauser, F. (2014), Storfjorden intraplate earthquake sequence, 2008-2014. (Unpublished).

Piepjohn, K., von Gosen, W., Läufer, A., McClelland, W. C. and Estrada, S. (2013), 'Ellesmerian and eurekan fault tectonics at the northern margin of ellesmere island (canadian high arctic)[ellesmerische und eurekan-störungstektonik am nordrand von ellesmere island (kanadische hocharktis).]', *Zeitschrift der Deutschen Gesellschaft für Geowissenschaften* **164**(1), 81–105.

Piepjohn, K., von Gosen, W. and Tessensohn, F. (2016), 'The eurekan deformation in the arctic: an outline', *Journal of the Geological Society* **173**(6), 1007–1024.

Pirli, M., Schweitzer, J., Ottemöller, L., Raeesi, M., Mjelde, R., Atakan, K., Guterch, A., Gibbons, S. J., Paulsen, B., Debski, W. et al. (2010), 'Preliminary analysis of the 21 february 2008 svalbard (norway) seismic sequence', *Seismological Research Letters* **81**(1), 63–75.

Pirli, M., Schweitzer, J. and Paulsen, B. (2013), 'The storfjorden, svalbard, 2008–2012 aftershock sequence: seismotectonics in a polar environment', *Tectonophysics* **601**, 192–205.

Polteau, S., Hendriks, B. W., Planke, S., Ganerød, M., Corfu, F., Faleide, J. I., Midtkandal, I., Svensen, H. S. and Myklebust, R. (2016), 'The early cretaceous barents sea sill complex: Distribution, 40 ar/39 ar geochronology, and implications for carbon gas formation', *Palaeogeography, Palaeoclimatology, Palaeoecology* **441**, 83–95.

Ramberg, I. B., Bryhni, I. and Nøttvedt, A. (2007), *Landet blir til: Norges geologi*, Norsk geologisk forening.

Richardsen, G., Vorren, T. O. and Tørudbakken, B. O. (1993), 'Post-early cretaceous uplift and erosion in the southern barents sea: a discussion based on analysis of seismic interval velocities', *Norsk Geologisk Tidsskrift* **73**(1), 3–20.

Roberts, D. (2003), 'The scandinavian caledonides: event chronology, palaeogeographic settings and likely modern analogues', *Tectonophysics* **365**(1), 283–299.

Sættem, J., Bugge, T., Fanavoll, S., Goll, R., Mørk, A., Mørk, M., Smelror, M. and Verdenius, J. (1994), 'Cenozoic margin development and erosion of the barents sea: core evidence from southwest of bjørnøya', *Marine Geology* **118**(3-4), 257–281.

Savostin, L. and Karasik, A. (1981), 'Recent plate tectonics of the arctic basin and of northeastern asia', *Tectonophysics* **74**(1-2), 111–145.

Skilbrei, J., Kihle, O., Olesen, O., Gellein, J., Sindre, A., Solheim, D. and Nyland, B. (2000), 'Gravity anomaly map norway and adjacent ocean areas, scale 1: 3 million', *Geological Survey of Norway, Trondheim* .

Steel, R. J. and Worsley, D. (1984), Svalbard's post-caledonian strata—an atlas of sedimentational patterns and palaeogeographic evolution, *in* 'Petroleum geology of the North European margin', Springer, pp. 109–135.

Tjåland, N. (2017), 'Double-difference relocation and empirical green's function analysis of storfjorden earthquakes'.

Torsvik, T. H., Van der Voo, R., Meert, J. G., Mosar, J. and Walderhaug, H. J. (2001), 'Reconstructions of the continents around the north atlantic at about the 60th parallel', *Earth and Planetary Science Letters* **187**(1), 55–69.

Vorren, T., Richardsen, G., Knutsen, S.-M. and Henriksen, E. (1990), The western barents sea during the cenozoic, *in* 'Geological History of the Polar Oceans: Arctic versus Antarctic', Springer, pp. 95–118.

Worsley, D. (2008), 'The post-caledonian development of svalbard and the western barents sea', *Polar Research* **27**(3), 298–317.